

Improving Wind and Power Predictions via Four-Dimensional Data Assimilation in the WRF Model: Case Study of Storms in February 2022 at Belgian Offshore Wind Farms

Tsvetelina Ivanova^{1,2}, Sara Porchetta^{3,4}, Sophia Buckingham⁵, Gertjan Glabeke^{1,6}, Jeroen van Beeck¹, and Wim Munters¹

¹Environmental and Applied Fluid Dynamics Department, von Karman Institute for Fluid Dynamics, Chau. de Waterloo 72, 1640 Rhode-Saint-Genèse, Belgium

²Department of Engineering Technology, Vrije Universiteit Brussel, Pleinlaan 2, 1050 Brussels, Belgium

³Civil and Environmental Engineering, Massachusetts Institute of Technology, 77 Massachusetts Avenue, 1-290, Cambridge, MA 02139, United States of America

⁴Department of Geoscience and Remote Sensing, Faculty of Civil Engineering and Geosciences, Delft University of Technology, Stevinweg 1, 2628 CN Delft, Netherlands

⁵Research & Innovation, ENGIE Laborelec, Rodestraat 125, 1630 Linkebeek, Belgium

⁶Department of Civil Engineering, Hydraulics Laboratory, Ghent University, Sint-Pietersnieuwstraat 41, B-9000 Gent, Belgium

Correspondence: Tsvetelina Ivanova (tsvetelina.ivanova@vki.ac.be)

Abstract. ~~Accurate wind and power predictions from numerical models are crucial for wind farm~~ Accurate modeling of wind conditions is vital for the efficient operation and management. ~~This study explores how these predictions can be improved of wind farms. This study investigates the enhancement of weather simulations~~ by assimilating local offshore LiDAR and/or SCADA data into a numerical weather prediction model, while ~~simultaneously taking into account~~ considering the presence of neighboring wind farms. ~~The focus is on~~ through wind farm parameterization. We focus on improving model output during storms impacting the Belgian-Dutch wind farm cluster located in the Southern Bight of the North Sea. ~~Our results show that for the current case study with extreme weather conditions, the assimilation of upstream data reduces mean absolute errors of wind speed,~~ via the four-dimensional data assimilation (nudging) technique in the WRF model. Our findings indicate that assimilating wind observations significantly reduces the relative root-mean-square error for wind speed at a wind farm located 47 km downwind from the offshore LiDAR platform. This leads to more accurate power production outputs. Specifically, at wind turbines experiencing wake effects, the wind ~~direction,~~ speed error decreased from 10.5 % to 5.2 %, and the wind direction error was reduced by a factor of 2.4. A proposed artificial cyclic configuration, leveraging the upwind LiDAR measurements showcases the potential for improving hour-ahead wind and power predictions, ~~up to 2.7 times in comparison to simulations without any assimilation.~~ This approach can be useful for forecasting purposes in short- to mid-term horizons, as well as for a long-term refined reanalysis of various weather conditions and events. Moreover, we perform a thorough sensitivity study to nudging parameters during versatile atmospheric conditions, which helps to identify best assimilation practices for this offshore setting. These insights are expected to refine wind resource mapping and the reanalysis of weather events, as well as to motivate more measurement campaigns offshore.

1 Introduction

20 In recent years, wind energy has emerged as a crucial and rapidly growing renewable energy source. Accurate predictions of wind speed, wind direction, and power production have become essential for efficient planning, design, and operation of wind farms. The use of numerical weather prediction (NWP) models, such as the open-source Weather Research and Forecasting Model (WRF; ~~Skamarock et al. (2019))~~ (Skamarock et al., 2019), developed at the National Center for Atmospheric Research (NCAR), plays a vital role in obtaining these accurate ~~predictions. In the context of wind farm market operations, forecasts~~
25 ~~of different lead times have different applications (Soman et al., 2010). Short-term forecasts of up to 6 hours ahead serve for regulation, dispatching, and congestion management, whereas mid-term forecasts of days-ahead serve for reserve requirement and market trading. Long-term forecasts of weeks, seasons or more, are useful for resource planning, operation management, optimal maintenance scheduling, and long-term energy trading. In the present study, short-term and mid-term forecasts are of interest. Furthermore, wind is generated due to a number of physical weather processes, which can be simulated accurately only~~
30 ~~by NWP models (Cheng et al., 2013). This renders the NWP approach more favorable for our goals than statistical models, although these can have strengths especially in post-processing techniques. For offshore wind farms~~predictions.

For weather simulations at offshore wind farm zones, NWP models do not necessarily have ~~initial conditions that are accurate enough sufficiently accurate initial conditions~~ due to the sparsity of offshore observations. This lack of data leads to broader issues, where NWP models can display large bias errors due to the overall lack of long-term offshore measurement data (Archer et al., 2014).

~~Extreme events~~ Furthermore, extreme events in which wind turbines are still operating can have a profound impact on wind farm operations; ~~since they~~. Such events involving high wind speeds can often lead to implications for power generation and grid stability. The impact at near-ground levels can be damaging for human activity, as well as cause grid instabilities and potential wind turbine cut-outs. ~~Consequently, numerous studies~~ This further increases the need for accurate weather
40 simulations. Numerous works are dedicated to studying and understanding extreme events, such as Larsén et al. (2019), Pryor and Barthelmie (2021), ~~Sethunadh et al. (2023), Vemuri et al. (2022)~~ Vemuri et al. (2022), Sethunadh et al. (2023). Given that extreme events are often influenced by the larger-scale dynamics of the atmosphere, NWP models are commonly employed to analyze and predict them. However, accurately capturing extreme events that significantly impact wind energy remains a challenge.

45 ~~Improvements in~~ Improving wind and power ~~predictions extend~~ simulations extends beyond model settings, and can be enhanced by incorporating additional physics. One such path to consider is the impact of wind farms on the atmosphere. In NWP models, wind farms ~~are~~ can be represented by a wind farm parameterization (WFP). Over the years, different ~~WFP~~ WFPs have been proposed. ~~A systematic literature review by Fischereit et al. (2022a) compares 10 existing WFPs. Another path for improving predictions is applying data assimilation (DA) techniques. In this study, we focus on both WFP and DA.~~ By
50 employing WFP, the influence of wind farms on the surrounding atmospheric conditions is accounted for, and consequently, an insight into approximated inter-farm dynamics is possible. ~~The WFP that is currently released in WRF is developed by Fitch et al. (2012), and models the wind farm as a momentum sink and a turbulent kinetic energy (TKE) source.~~ A study by

Lee and Lundquist (2017) quantifies wind and power prediction improvements that are achieved by incorporating ~~this~~-WFP. A systematic literature review by Fischereit et al. (2022a) compares 10 existing WFPs. Furthermore, Fischereit et al. (2022b) ~~highlight highlights~~ that the WFP of Fitch et al. (2012) is a suitable state-of-the-art choice for modeling the presence of wind farms in WRF, and is selected in the present work. ~~Overall, WFP has been used in a variety of applications, including This WFP models the wind farm as a momentum sink and a turbulent kinetic energy (TKE) source. Other WFP applications include~~ wind-wave coupling studies ~~(Porchetta et al., 2021), and assessment of modifications in near-surface environment of thunderstorm outflow boundaries (Tomaszewski and Lundquist, 2021).~~, such as Porchetta et al. (2021). Accurately capturing atmospheric conditions is crucial for modeling wind farm wakes. However, when representing wind farm wakes in mesoscale models using WFP, uncertainties arise (Eriksson et al., 2017; Peña et al., 2022; Ali et al., 2023). WFP has limitations, including the need for TKE correction, as well as its sensitivity to atmospheric stability. Additionally, WFPs restrict options for planetary boundary layer schemes in NWP models, which in turn affects the fidelity of boundary layer representation.

Along with model setting and including more physics within WRF, improvements in wind and power ~~predictions model~~ output can also be achieved ~~via DA~~ by employing data assimilation (DA) techniques. Data assimilation is the process of integrating observed data into a numerical model (Skamarock et al., 2019). We ~~will~~ distinguish between two groups of such techniques: variational DA (Barker et al., 2012) and four-dimensional data assimilation (FDDA or nudging, Liu et al. (2008)). Variational DA is concerned with finding the optimal initial state of the atmosphere (in the case of three-dimensional variational data assimilation (3DVar), Barker et al. (2004)), ~~or and furthermore,~~ with finding the optimal model trajectory based on this optimal initial state (in the case of four-dimensional variational data assimilation (4DVar), Huang et al. (2009); Zhang et al. (2013, 2014)). Both 3D and 4D variational techniques rely on minimizing the difference between model forecasts and observations by optimizing a cost function. One work that exploits the benefits of variational data assimilation is by Sun et al. (2022), in which wind speed forecasts are improved when assimilating observations from the nacelle of turbines. In contrast, FDDA (nudging) operates differently from variational data assimilation: FDDA directly influences the state variables over time in order to match observed data (Reen, 2016), and it is the selected method in this work. In FDDA, the approach is to introduce tendency terms in the model equations to adjust the prognostic variables, such as temperature, humidity, and wind components, towards observed values. This approach acts as a controller, rather than a cost function optimizer. This makes FDDA much more computationally efficient than variational methods, and this is highly relevant in an operational context (Cheng et al., 2017). A drawback of this method is that only prognostic model variables can be assimilated. Besides observational FDDA/nudging, it is also possible to perform grid nudging and spectral nudging in WRF ~~(Skamarock et al., 2019)~~: these are out of the scope of this work. Several studies have explored the leverage of data assimilation techniques in mesoscale models for wind energy applications. For example, Kosovic et al. (2020) use RTFDDA (real-time FDDA) for local data, integrated with ~~artificial intelligence approaches regarding the conversion from wind to power via machine learning—a machine learning approach for power estimation.~~ Nudging techniques are also applied in the onshore study of Cheng et al. (2017) that highlights the effectiveness of ~~FDDA RTFDDA (within a customized version of WRF)~~ in improving wind energy predictions ~~0-3 0-3~~ hours ahead for normal weather conditions, using only wind speed observations from wind turbine ~~(WT) anemometers. In that study, the RTFDDA forecasting system is used, and as a NWP model, a customized version of WRF is utilized. anemometers.~~

Furthermore, the study of Mylonas et al. (2018) performs FDDA nudging of observations from the offshore meteorological mast FINO3 in the North Sea for wind resource assessment and reanalysis.

90 ~~Despite the vast research available, to our knowledge, there is no study that combines the benefits~~ Our research presents a novel approach to improving wind and power model output by integrating the advantages of a physics-based WFP and FDDA ~~of local observations offshore in improving wind and power predictions in WRF. This is why we in WRF, particularly during extreme offshore conditions.~~ We focus on utilizing ~~FDDA in WRF offshore by performing observational FDDA nudging~~ observational FDDA of horizontal wind components, ~~derived from wind speed and wind direction.~~ The latter are collected by ~~gathered from a LiDAR (Light Detection and Ranging) profilers, and SCADA (Supervisory Control And Data Acquisition) of wind turbine anemometers at hub height. Furthermore, having prominently situated upstream observations makes FDDA especially advantageous as it provides~~ vertical profiler. This approach is unique in its offshore application of FDDA in WRF ~~due to the strategic placement of the LiDAR upstream (with respect to the most common South-Westerly winds in the Southern Bight of the North Sea). This geographical advantage allows for advanced~~ information on incoming wind conditions in advance, ~~which will be highlighted in this work. With this strategy, we aim to enhance~~ to be provided approximately one hour ahead, ~~which is the advective time required. Our goal is to improve~~ the accuracy of wind and power ~~predictions offshore during extreme events that occurred~~ model output offshore by assimilating this data during significant events such as the storms Eunice and Franklin in February 2022 over the Belgian North ~~sea, namely the storms Dudley, Eunice and Franklin~~ Sea. These events had a ~~significant~~ substantial impact on wind power production (reported ~~for example,~~ for example, in Belgian Offshore ~~Platform News (2022)), making them~~ important crucial case studies for ~~exploring possibilities for improving wind and power production predictions. Moreover, in order our research. Furthermore,~~ to gain insight into ~~the FDDA setting, we consider~~ optimal FDDA settings for this offshore configuration, we experiment with sensitivity to different observational nudging parameters ~~by varying, such as~~ nudging strength and horizontal radius of influence of the assimilated observations. ~~To evaluate and verify~~ We evaluate the performance of the simulations, ~~the results are compared to SCADA by comparing the results~~ to LiDAR and SCADA (Supervisory Control And Data Acquisition) datasets, using classic metrics from the state-of-the-art ~~handbook on wind forecasting by Yang et al. (2021). These metrics are MAE (mean absolute error), RMSE (root-mean-square error), and bias with respect to observations.~~

The paper is structured as follows. Section 2 describes the methodology and the configuration of the numerical setup of the WRF model ~~including the FDDA algorithm, the available offshore observations, and selected case studies for simulations in~~ this work. Section 3 ~~portrays results for different scenarios, and the predictions are verified using MAE (mean absolute error) with respect to observations. Section 4 expresses~~ expresses the results and discussion for the different simulation scenarios. ~~Finally, Sect. 4 outlines~~ the conclusions of this paper.

2 Methodology and numerical setup

The NWP model employed in this work is the Advanced Research WRF (ARW) Model ~~(Skamarock et al., 2019), v~~ (Skamarock and Klemp, ~~version~~ 4.5.1, which is a state-of-the-art mesoscale NWP system available in the public domain. It solves the fully com-

pressible non-hydrostatic Euler equations. ~~WRF, and it~~ has a rich set of physics parameterizations, ~~and has an implemented algorithm to assimilate prognostic model variables such as the horizontal components of wind speed via the FDDA (nudging) technique, as described in Skamarock et al. (2019) and Reen (2016). With this algorithm, the numerical solution is nudged towards observations by introducing tendency terms in the model equations as~~

$$125 \quad \frac{\partial q\mu}{\partial t}(x, y, z, t) = F_q(x, y, z, t) + \mu G_q \frac{\sum_{i=1}^N W_q^2(i, x, y, z, t)(q_o(i) - q_m(x_i, y_i, z_i, t))}{\sum_{i=1}^N W_q(i, x, y, z, t)},$$

where q is the quantity being nudged (in this work, horizontal wind components derived from wind speed and wind direction), μ is the dry hydrostatic pressure, F_q are the physical tendency terms of q , G_q is the nudging strength, N is the total number of observations, W_q is the weighing function in space and time, q_o is the observed value of the quantity of interest, and $q(x_i, y_i, z_i, t)$ is its model value. The working principle is of a proportional controller: with the approaching of the model value to its observed value, the nudging tendency term decreases. ~~~~~

2.1 The WRF model configuration

Our study is focused on the Belgian-Dutch wind farm cluster. The setup consists of five nested domains, three of which are identical and innermost. The domains have their names and grid cells as follows. D01: 150×150 ; D02: 190×190 ; D03, D04, and D05: 220×190 grid cells; centered at latitude 51.42° N and longitude 2.74° E, with one-way nesting. The [Lambert conformal projection is selected](#). ~~The~~ three identical innermost domains ~~will be are~~ of main interest, with a size of ~~680-680~~ km by ~~596-596~~ km. The horizontal grid spacing is ~~18-18~~ km for the outer domain, ~~6-6~~ km for the intermediate domain, and ~~2-2~~ km for the three innermost domains. The latter follows the guidelines of Fischereit et al. (2022a) to use horizontal grid spacing of at least ~~3 to 5~~ ~~3 to 5~~ times the wind turbine rotor diameter for the domains ~~where the WFP is active with active WFP~~ (in this case, ~~the innermost ones~~). ~~We run the simulations using D04 and D05). We configure the simulations for~~ the three identical domains (with ~~2-2~~ km grid spacing) in the following way: D03 is for simulations without WFP, D04 is for active WFP, and D05 – for active WFP ~~and while~~ performing FDDA. The domains are shown in Fig. 1, along with key [measurement locations](#) of three LiDARs: at the Westhinder (WHi) platform (Glabek et al., 2023), and at the Lichteiland Goeree platform (LEG) and Europlatform (EPL) (Wind@Sea project, Wind Energy Research Group at TNO Energy Transition, 2023). ~~Details on the physics~~

145 ~~The setup in this work is based on Hahmann et al. (2020), Dörenkämper et al. (2020), and Larsén and Fischereit (2021). Relevant details on the~~ parameterizations used in the setup can be found in Table 1, ~~and it is based on Hahmann et al. (2020), Dörenkämper et al. (2020), and Larsén and Fischereit (2021). The Lambert conformal projection is selected. The~~ ~~The~~ cumulus scheme is used only on the outermost domain. ~~The purpose of our work offshore with FDDA and with~~ ~~Our study involves usage of~~ the WFP of Fitch et al. (2012), ~~which~~ further requires the introduction of sufficient vertical model levels ~~in order to have~~. ~~This allows~~ a representative description of the wind profile across the rotor, which is done by relying on recommendations from Lee and Lundquist (2017). ~~The TKE advection flag has been switched on, following the recommendations of Areher et al. (2020). The vertical levels are stretched, which ensures more levels close to the surface. The total number of~~

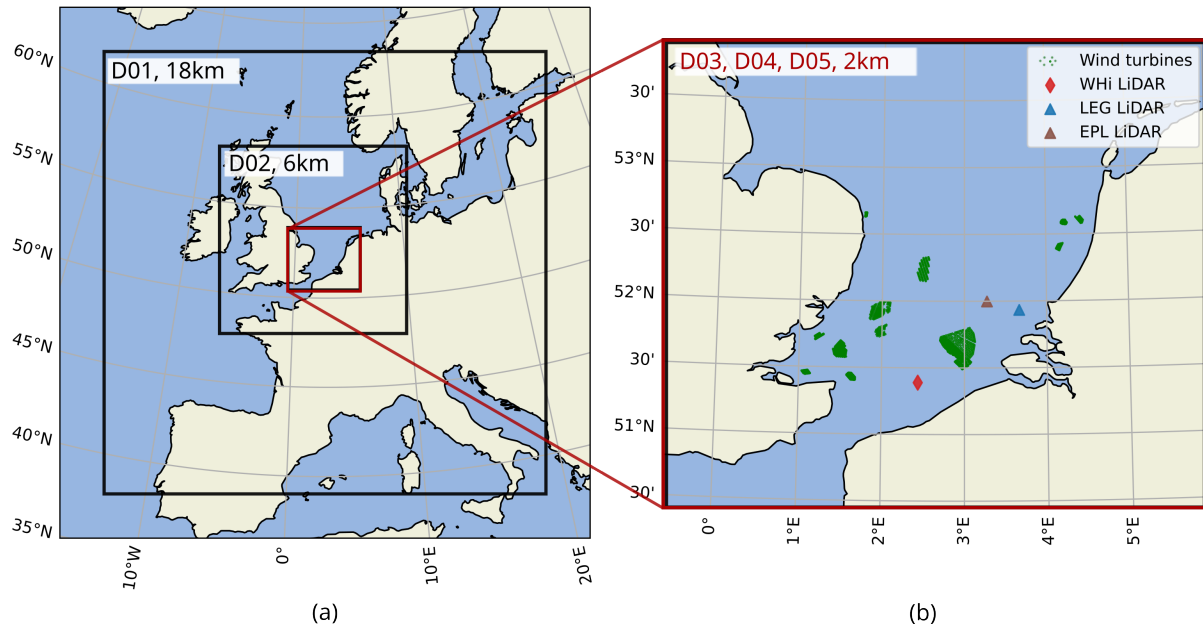


Figure 1. Nested domains in WRF (a). The domains of interest (b) are the three identical D03, D04, D05, with a grid spacing of 2 km. Key measurement locations are indicated (i.e. WHi LiDAR, LEG and EPL LiDARs). The 1409 wind turbines that are currently included in the WRF setup are also visualized in (b).

levels is 80 (Lee and Lundquist, 2017). The lowest level is at 6 m, with sufficient points across the wind turbine rotor for a typical offshore wind turbine (WT) in the Belgian-Dutch cluster. More specifically, for the smallest wind turbine within the Belgian side of the Belgian-Dutch cluster, there are 8 vertical levels that span across the rotor, whereas for the largest wind turbine of this cluster, there are 15 levels. The model pressure top is at 1000 Pa.

~~In order to account for farm effects, the~~ To consider the impact of wind farms, we incorporate not only the Belgian-Dutch wind farm cluster, but also the fully-commissioned offshore wind farms of interest in the North Sea are also included in our simulations in the South Bight of the North Sea via the WFP of Fitch et al. (2012) in WRF within the WRF model. This group of wind farms consists of 1409 wind turbines (out of 5779 in total in Europe and UK (Hoeser et al., 2022)) within 27 different wind farms that are represented in the setup, in proximity to the Belgian-Dutch cluster. The locations of these wind farms are extracted from Hoeser et al. (2022), and the publicly available dataset of Hoeser and Kuenzer (2022). The details of the different wind farms are summarized in Appendix A, Table A1. Besides wind turbine locations, the WFP requires the power and thrust curves for each wind turbine in order to simulate its effects on the atmosphere. These were obtained from a mix of both open (<https://www.thewindpower.net/>; and WindPRO (EMD-International)), and confidential sources.

~~The vertical levels are stretched which ensures more levels close to the surface, and there are 80 levels in total (Lee and Lundquist, 2017). The lowest level is at 6 m, with sufficient points across the wind turbine rotor for a typical offshore wind turbine in the~~

Table 1. Parameterization options and configuration in the present WRF setup

Parameterization	Scheme (with option in namelist)	Reference
PBL scheme	MYNN 2.5 level TKE (option 5)	Nakanishi and Niino (2006)
Cumulus	Kain-Fritsch (option 1)	Kain (2004)
Microphysics scheme	Thompson et al. (option 8)	Thompson et al. (2008)
Radiation	RRTMG (option 4)	Iacono et al. (2008)
Land surface model	NOAH LSM (option 2)	Ek et al. (2003)
<u>Wind farm parameterization</u>	<u>when active: Fitch (option 1)</u>	<u>Fitch et al. (2012)</u>
<u>TKE correction coefficient α</u>	<u>0.25 (default value)</u>	<u>Archer et al. (2020)</u>

~~Parameterization options in the present WRF model configuration~~

~~Belgian-Dutch cluster. The model pressure top is at 1000 Pa. The performed WRF simulations take into account the TKE advection with a correction factor α of 0.25, following Archer et al. (2020). This coefficient α is denoted in Table 1.~~

170 For time integration, a third order Runge-Kutta scheme is used, and for advection – ~~second~~ – ~~to sixth order~~ second- to sixth-order spatial discretization schemes. For the model integration, adaptive time stepping is used, with a target Courant–Friedrichs–Lewy number of 0.6. For initial and boundary conditions, the Global Forecast System (GFS) 3-hourly data from NCEP’s Historical Archive is used, with forecast grids on a 0.25 by 0.25 global latitude longitude grid (National Centers for Environmental Prediction, National Weather Service, NOAA, U.S. Department of Commerce, 2015). ~~The simulated time is from 15 February 2022 to 22 February 2022 including~~ All simulated periods include a 12-hour spin-up time. ~~This week includes three extreme events which are~~ These periods of interest are detailed in Sect. 2.3 and include extreme events in February 2022 (storms Eunice and Franklin).

180 Our study investigates the sensitivity of results to nudging parameters. Varying such parameters helps to gain insight into the most suitable assimilation strategies for this offshore configuration. For a selected day (17 February 2022), a number of simulations are performed by varying the horizontal radius of influence R_{xy} , as well as the nudging strength G_q . In these numerical experiments, either LiDAR or SCADA data is assimilated. The FDDA algorithm is detailed in Sect. 2.2. The full sensitivity experiment is described in Sect. 2.5.

~~Nested domains in WRF. The domains of interest are the three identical D03, D04, D05, with a grid spacing of 2. Key locations that contain observations are indicated (i.e. Westhinder (WHi) LiDAR, LEG and EPL LiDARs). The 1409 wind turbines that are currently included in the WRF setup are also shown on the right.~~

2.2 The FDDA (nudging) algorithm

190 ~~Additionally, our study investigates different configurations for FDDA with respect to data sources (either LiDAR or SCADA), and the sensitivity of results in one day (17 February, with 12-hour spin-up time also included in this day) to the following nudging parameters: horizontal~~ WRF has an implemented algorithm to assimilate prognostic model variables such as the horizontal components of wind speed via the FDDA technique, as described in Skamarock et al. (2019) and Reen (2016). With

this algorithm, the numerical solution is nudged towards observations by introducing tendency terms in the model equations as

$$\frac{\partial q\mu}{\partial t}(x, y, z, t) = F_q(x, y, z, t) + \mu G_q \frac{\sum_{i=1}^N W_q^2(i, x, y, z, t)(q_o(i) - q_m(x_i, y_i, z_i, t))}{\sum_{i=1}^N W_q(i, x, y, z, t)},$$

195 where q is the quantity being nudged (in this work, horizontal wind components that are projected from wind speed and wind direction observations, as in Cheng et al. (2017)), μ is the dry hydrostatic pressure, F_q are the physical tendency (or model forcing) terms of q , G_q is the nudging strength, N is the total number of observations, W_q is the weighing function in space and time, q_o is the observed value of the quantity of interest, and $q(x_i, y_i, z_i, t)$ is its model value. The working principle is of a proportional controller: with the approaching of the model value to its observed value, the nudging tendency term decreases.

200 The weighing function W_q can be expressed as the product of horizontal (w_{xy}), vertical (w_σ), and temporal (w_t) contributions (Xu et al., 2002). The contribution w_{xy} is a function of the horizontal radius of influence R_{xy} , and nudging strength G_q . The w_σ is the vertical weighing function, and w_t is a function of the assimilation time window is set as default $\tau = 0.667$ hours (Skamarock et al., 2019). Varying the nudging radius and strength can help gain insight into suitable assimilation strategies and practices for extreme event forecasting in wind energy applications τ over which an observation is used in the nudging algorithm. The horizontal weighing function is a Cressman-type function given by

$$205 \quad w_{xy} \equiv \frac{R_{xy}^2 - D^2}{R_{xy}^2 + D^2}, \quad 0 \leq D \leq R_{xy},$$

$$w_{xy} \equiv 0, \quad D > R_{xy},$$

where R_{xy} is the radius of influence and D is the distance from the observation location to the grid point. The vertical and the temporal weighing functions are also distance-weighted. Further details on observational nudging can be found in Grell et al. (1994) and in Xu et al. (2002).

210 In this work, we perform a sensitivity study to the horizontal radius of influence R_{xy} , as well as to the nudging strength G_q . This study is described in Sect. 2.5 with all tested nudging parameter values.

2.3 Available offshore observations

215 ~~The observations used for assimilation and performance evaluation of the simulations are~~ In this section, we detail all offshore observations that are used in this work, both for assimilation in WRF, and for simulation performance evaluation. The locations of all offshore observations are indicated in Fig. 2(a).

LiDAR profiler at the Westhinder platform (WHi)

220 The observations used for assimilation are collected by a vertical LiDAR profiler at the Westhinder survey platform (with coordinates $51^\circ 23' 18.74''\text{N}$, $02^\circ 26' 16.18''\text{E}$), as well as by cup anemometers at the wind turbines' nacelles (SCADA data) that belong to one of the wind farms in the Belgian-Dutch cluster. The vertical profiling LiDAR (ZX 300M) is installed at that shown in Fig. 2(b). It has been installed at the Westhinder platform since August 2021 and has been collecting wind speed

and wind direction information since (Glabeke et al., 2023). ~~The LiDAR location is illustrated in Fig. 2: located upstream from the farm of interest, the Westhinder LiDAR is situated at approximately 42 from the Belgian-Dutch cluster. It~~ In this study, we utilize WHi LiDAR data that is available from 4 August 2021 to 18 July 2022, as well as from 26 January to 6 February 2023. This LiDAR measures at 11 different heights (34.5, 44.5, 62.5, 79.5, 104.5, 124.5, 149.5, 174.5, 224.5, 274.5 and 324.5 mTAW), as shown in Fig. 2(c). The measurement heights are in mTAW (meters Tweede Algemene Waterpassing), which means that the average sea level at low tide in Ostend (Belgium) is used as the zero level. This value for Ostend is ± 2.3 m) at ± 1 (positive and negative deviations) with respect to the mean sea level. The LiDAR is retrieving wind vector data at a frequency of 1 Hz per height. A full measurement of the vertical profile typically takes 17 seconds due to the extra time for beam focus adjustment, as well as for additional weather condition measurements used in quality control. Thus, for a 10-minute interval, the maximum number of validated wind speed and wind direction measurements is 35. The validation is based on a wind-industry filtering, performed by the LiDAR software (User's Manual ZephIR, 2018), as meteorological conditions can result in non-validated wind data (for example, due to low cloud ceiling, fog, or precipitation). The filtering criteria are selected based on a DNV (Det Norske Verita) classification.

The location in which ~~these~~ the WHi LiDAR observations are collected is especially favorable, ~~as~~ since the measurements are of free-stream wind, given the predominant South-Westerly winds (shown in the year-long wind rose in Fig. 2) ~~(d)~~. This allows information to propagate towards the farm of interest when performing FDDA of these local observations. ~~In contrast, the SCADA collects~~ The typical advection timescale of this propagation is approximately one hour. Therefore, the assimilation of such upwind data can help improve hour-ahead predictions. This approach is discussed in Sect. 2.5, and the results – in Sect. 3.1.

240 SCADA from nacelle anemometers at Front & Waked WTs

The nacelle anemometers gather in-situ data on horizontal wind speed and wind direction at the wind farms on power production, in addition to horizontal wind speed and wind direction. In the present work, we consider 10-minute averages of both SCADA and LiDAR datasets, which both otherwise have a one-second temporal resolution. In order for these observations to be assimilated into WRF, the wind speed and wind direction from the LiDAR and the SCADA at hub heights is pre-processed and translated to horizontal wind components via a standard procedure (Cheng et al., 2017). Additionally, the SCADA system records power production data. For the purpose of our simulations, we have specifically selected two locations within the Belgian-Dutch cluster (which comprises 572 wind turbines) as depicted in Fig. 2. The first location, referred to as “Front WTs”, includes a subset of five wind turbines. These turbines are strategically positioned in the front row, aligning with the most common wind direction from the South-West. This alignment is consistent both for the period under investigation and for the overall wind direction in the Belgian North Sea, as shown from the wind rose in Fig. 2(d). The second location, “Waked WTs”, consists of another subset of five wind turbines. These turbines are situated in the wake, on an arbitrary back row, of a selected Belgian wind farm (when the wind direction is from the South-West). The selection of these two distinct locations allows us to observe the effect of the wind farm parameterization across a few kilometers. It also enables the assessment of the area of impact of the data assimilation upwind.

255 ~~Locations of interest within the innermost domains: the (typically) upstream WHi LiDAR; the “Front WTs” and “Waked~~
~~WTs” from the Belgian-Dutch cluster (two subsets of 5 wind turbines each); the LEG and EPL LiDARs. An illustration of~~
~~the LiDAR with respect to a typical wind turbine is shown. On the right: a wind rose obtained from the LiDAR dataset of~~
~~Glabeke et al. (2023) at 104.5 above sea level for a period of almost one year (4 August 2021 to 18 July 2022). The reason for~~
~~selecting exactly five turbines per location (Front WTs and Waked WTs) is the computational domain of our simulations. Each~~
260 ~~subset of turbines is located within a specific computational cell with a grid spacing of 2 km. Therefore, for both locations, we~~
~~consider the average values from the SCADA of the corresponding five turbines, providing us with a representative sample for~~
~~each computational cell. However, due to a non-disclosure agreement with the wind farm operator, we are unable to list the~~
~~exact coordinates of these turbines.~~

LiDAR at the Lichteiland Goeree (LEG) platform

265 To further evaluate our numerical results, we compare ~~also with a LiDAR~~ them additionally to a LiDAR profiler on the
Lichteiland Goeree (LEG) platform (coordinates 51°55'30" N, 3°40'12" E) provided by the Wind@Sea project, Wind Energy
Research Group at TNO Energy Transition (2023) (<https://www.tno.nl/>, <https://nimbus.windopzee.net/>). The LEG platform
~~is positioned at approximately 30~~ collects meteorological observations and is positioned approximately 110 km ~~South-West~~
~~from Hoek van Holland, and it collects meteorological observations.~~ away from the Westhinder platform as shown in Fig.
270 2(a). Wind speed observations are ~~available and~~ obtained via a Leosphere Windcube LiDAR V2.1 which can measure up to
approximately ~~250-240~~ m above sea level (8 different heights at 62, 90, 115, 140, 165, 190, 215 and 240 m above sea level)
~~. This LiDAR is located approximately 63 further downstream the Belgian-Dutch cluster (see Fig. 2). Finally, we perform~~
~~comparisons simultaneously with a wind vector data rate of 1 Hz.~~

LiDAR at the Europlatform (EPL)

275 We perform comparisons of simulations with one more LiDAR ZX-300M wind profiler dataset that is collected at the Eu-
roplatform (EPL) also by the Wind@Sea project, Wind Energy Research Group at TNO Energy Transition (2023)(~~,-~~). The
measurement heights of the EPL LiDAR are 63, 91, 116, 141, 166, 191, 216, 241, 266 and 291 meters. This platform is ~~also~~
~~located at about 30 South-West from Hoek van Holland.~~ located in proximity to the LEG platform, as indicated in Fig. 2(a).

2.4 Case studies of extreme events at specific locations

280 ~~The period of interest in this research is from 15-~~

Performance metrics

The WHi LiDAR and SCADA datasets (at Front & Waked WTs locations) are utilized for assimilation (nudging) in WRF in
distinctive numerical experiments (described in Sect. 2.5), as well as for model output evaluation. Before assimilation in WRF,
all wind speed and wind direction observations are projected onto the axes aligned with model U and V velocity variables

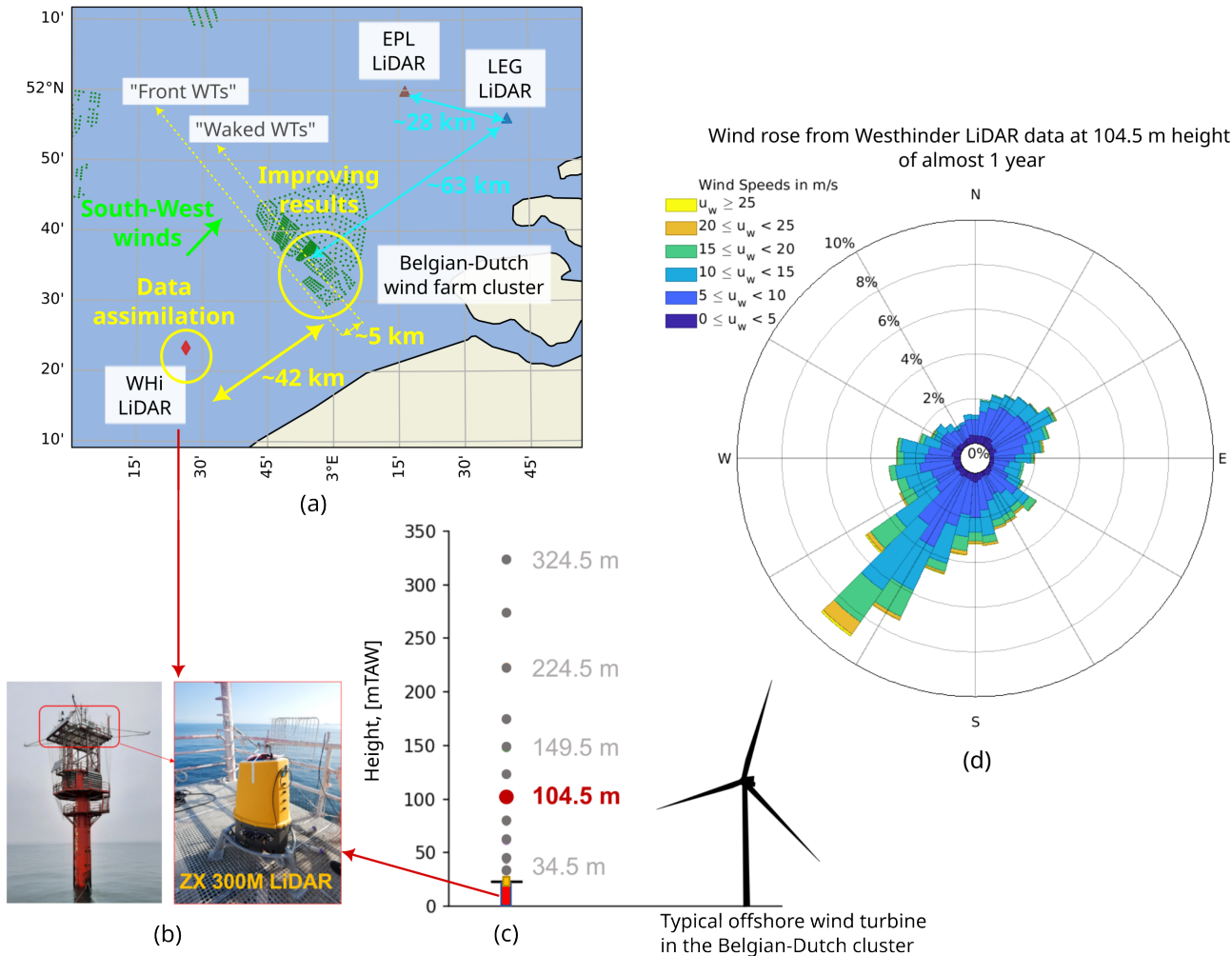


Figure 2. Locations of interest (a) within the innermost domains: the (typically) upstream WHi LiDAR; the Front WTs and Waked WTs from the Belgian-Dutch cluster; and the LEG and EPL LiDARs. The WHi LiDAR is shown on its platform (b), as well as its illustration with respect to a typical wind turbine (c). Finally, a wind rose (d) obtained from the LiDAR dataset of Glabeke et al. (2023) at 104.5 mTAW for a period of almost one year (4 August 2021 to 18 July 2022).

285 (Cheng et al., 2017). The results obtained from simulations are compared to the five locations in total, shown in Fig. 2: three
 LiDARs (WHi, LEG, and EPL), as well as two locations (Front & Waked WTs) with wind turbine data (local wind speed, wind
 direction, and power) from a SCADA database.

To evaluate the performance of simulations, we utilize established metrics, outlined in Yang et al. (2021). These metrics
 include Mean Absolute Error (MAE) (Lydia et al., 2014), Root-Mean-Square Error (RMSE) (Zhao et al., 2011), and Bias
 290 (Wang et al., 2019). Each of these metrics provides a different perspective on the accuracy of our simulations compared to
 offshore observations. Let us denote the i th (normalized) model output variable as $p_{m,i}^i$, the i th (normalized) observed variable

as p_o^i , and the length of the data set as N . The MAE is a widely used metric for evaluating wind model output, as it reflects the overall error level. It is calculated as the average absolute difference between the model output and the observed data:

$$\text{MAE} = \frac{1}{N} \sum_{i=1}^N |p_m^i - p_o^i|.$$

295 The RMSE is another important metric, particularly due to its sensitivity to outliers in NWP model output. It is computed as the square root of the average squared differences between the model output and the observed data:

$$\text{RMSE} = \sqrt{\frac{1}{N} \sum_{i=1}^N (p_m^i - p_o^i)^2}.$$

Lastly, the bias indicates the average deviation of the model output from the actual observed values:

$$\text{Bias} = \frac{1}{N} \sum_{i=1}^N (p_m^i - p_o^i).$$

300 These metrics allow a comprehensive analysis and evaluation of model performance across different simulation scenarios.

2.4 Case studies of different weather conditions

The case studies of interest are described in Table 2. For an easier reference throughout the text, these cases are labeled as time frames F1 to F4. All four cases have a suitable South-West wind direction that allows the advection of the assimilated LiDAR data towards the Belgian-Dutch cluster (Fig. 2(a)). Each case study has a targeted goal. F1 enhances model accuracy using FDDA. F2 involves a comprehensive sensitivity analysis to nudging parameters, which is one of the main goals of this work. F3 displays a negative wind speed bias when WFP is inactive, a condition that deteriorates with the activation of WFP due to further momentum extraction from an already underpredicting baseline. Conversely, F4 displays a positive wind speed bias when WFP is inactive, which is reduced once WFP is activated. Thus, for both F3 and F4, incorporating FDDA is explored to enhance model output. All times indicated throughout the text and figures are in UTC time zone.

310 Time frame F1 includes two storms (Eunice and Franklin) in February 2022. ~~In this period, three extreme events occurred in the Belgian North-Sea: the storms Dudley, Eunice, and Franklin. Note that hours in this text and all graphs are always in local time (UTC +1). At the Westhinder (WHi) LiDAR~~ The goal within F1 is to use FDDA (of upwind LiDAR) to help improve model performance. For F1 at the WHi LiDAR location, according to the observations in Fig. 3, at 104.5 height, these mTAW height, the storms have the following characteristics:

- 315
- Storm ~~Dudley: afternoon of 16 February—afternoon of 17 February, with a peak velocity of 25.81 at 21h on 16 February 2022.~~
 - ~~Storm Eunice: Eunice occurred from the~~ early morning of 18 February ~~—to the~~ early morning of 19 February, ~~with~~ . It reached a peak velocity of 37.13 at 14h m s^{-1} at 14:00 on 18 February 2022. ~~Wind direction is overall gradually transient~~ 2022, with the wind direction varying between 225 and 275 degrees.

Table 2. Time frames of interest in this study along with their corresponding goals.

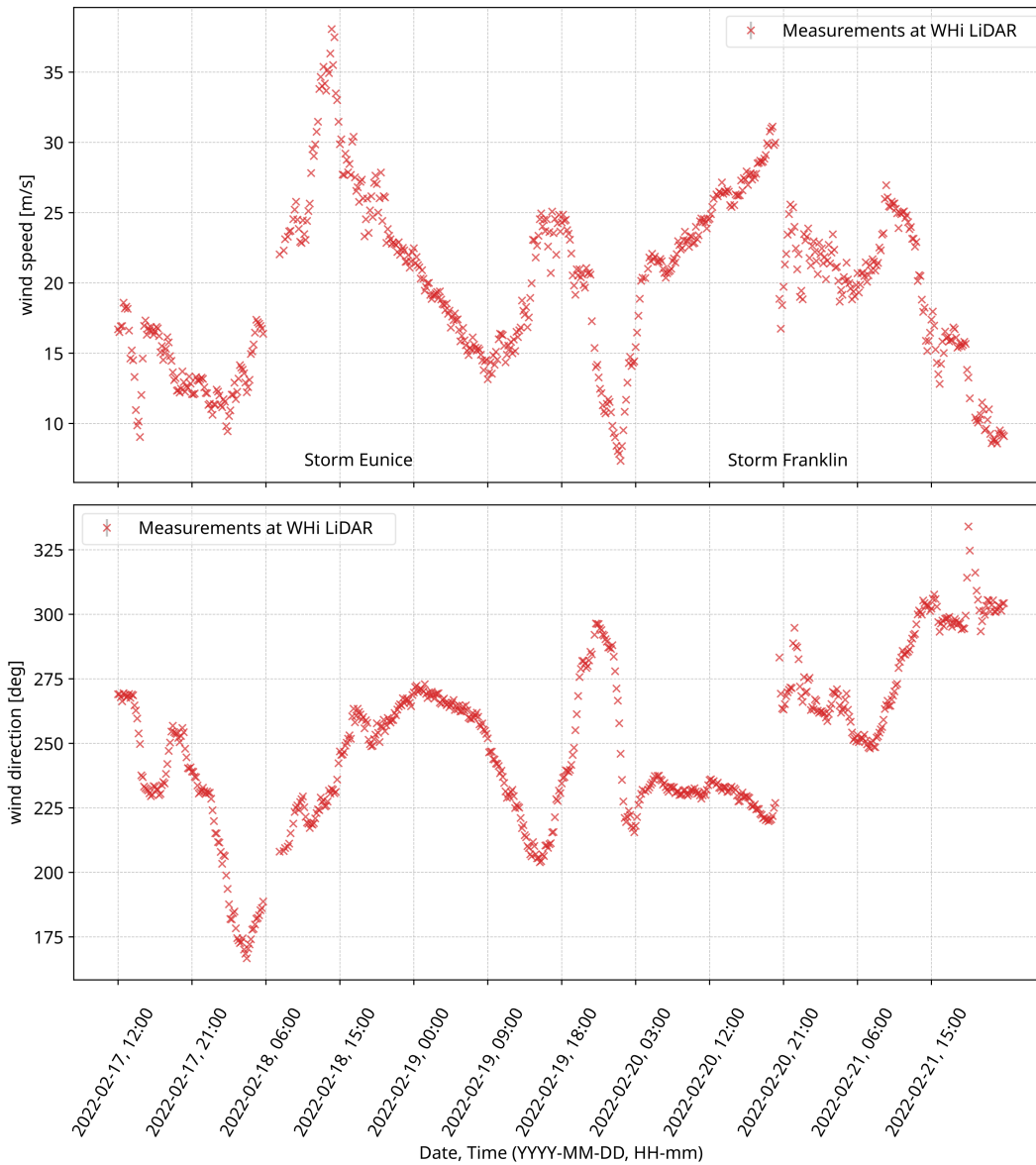
<u>Label</u>	<u>(Duration) Time frame dates</u>	<u>Goal</u>
<u>F1</u>	<u>(4 days) 17 February 2022 to 21 February 2022</u>	<u>Improve model performance via FDDA of local upwind LiDAR data at a specific height</u>
<u>F2</u>	<u>(1 day) 17 February 2022 – 18 February 2022</u>	<u>Sensitivity study of nudging strength and horizontal radius of influence to identify optimal FDDA practices</u>
<u>F3</u>	<u>(2 days) 20 October 2021 – 22 October 2021</u>	<u>Assess FDDA performance when the wind speed bias is negative (for inactive WFP)</u>
<u>F4</u>	<u>(4 days) 30 January 2023 – 3 February 2023</u>	<u>Test FDDA when the wind speed bias is positive (for inactive WFP), that also involves notable wind speed fluctuations.</u>

320 – Storm Franklin ~~spanned from the~~ afternoon of 20 February ~~noon at to noon on~~ 21 February, ~~with peak velocity.~~ The peak velocity recorded up to 30.46 at 19h30-m s⁻¹ at 19:30 on 20 February 2022. Wind speed and wind direction undergo sharp transitions. Notably, both the wind speed and direction underwent significant changes, especially from ~~20h00 to 20h30~~ 20:00 to 20:30 on 20 February 2022.

~~We selected this week-long period as it provides~~

325 The selection of the F1 period is strategic, given its versatile atmospheric conditions, ~~including times with values around.~~ This period includes instances with wind speeds around the cut-out wind speed value, as well as periods featuring fast times featuring rapid changes in wind direction, ~~which can lead to yaw misalignment, making this an interesting case study for FDDA. Data assimilation (FDDA/~~ Four-dimensional data assimilation (nudging) is favorable whenever the wind direction is predominantly from South-West, as this allows for the Westhinder LiDAR to be upstream upwind from the Belgian-Dutch cluster. This is indeed most often the case in the Southern Bight of the North Sea, as shown in the wind rose in Fig. 2(d). The average wind direction for F1 is West-Southwest. ~~Moreover, the LiDAR observations~~ Note that gaps in the time series in Fig. 3 ~~evaluate that the average wind direction is from West-Southwest (247.52) for the selected week in February 2022, which is suitable to demonstrate the FDDA capabilities of upstream local data.~~

335 ~~The results obtained from the simulations are compared to the five shown locations in Fig. 2: three LiDARs (WHi, LEG, and EPL), as well as two locations with wind turbine data (local wind speed, wind direction, and power) from a SCADA database. The two different locations within the Belgian-Dutch cluster (containing 572 wind turbines) in Fig. 2 are as follows. The first location, “Front WTs”, contains a subset of 5 wind turbines considered as front row with respect to the most common wind direction from South-West (both for the investigated period and overall for the Belgian North Sea, as mentioned previously). The second location, “Waked WTs”, consists of another subset of 5 wind turbines, but they are positioned in the wake~~ (arbitrary back row of a selected Belgian wind farm). In both cases, we consider the average values from the SCADA of ~~the corresponding 5 wind turbines. Having comparisons both in the front and in the wake allows observing the effect of the~~



Time-series of the LiDAR observations at 104.5 height during the three extreme events from the Westhinder (WHi) dataset of Glabeke et al. (2023).

Figure 3. Time frame F1: LiDAR observations at 104.5 mTAW height from the Westhinder (WHi) dataset of Glabeke et al. (2023). UTC timezone.

wind farm parameterization across a few kilometers, as well as the area of impact of the data assimilation upstream, are due to data filtering performed by the LiDAR software based on meteorological conditions.

2.5 Baseline simulations and numerical experiments

345 Time frame F2 is a selected day from F1 (17 February 2022), in which we focus on a sensitivity study of the nudging strength and radius of influence to identify optimal FDDA practices. This procedure is detailed in Sect. 2.5. The goal in F2 is to understand how different parameters of the FDDA algorithm impact model performance and accuracy, and to identify best FDDA practices for the offshore setting.

~~The storms are illustrated in a timeline in Fig. 4. We divide the study in two time frames~~ Time frame F3 spans over two days,
350 from 20 October 2021 to 22 October 2021. During this period, we aim to demonstrate the capabilities of a selected FDDA setting (based on the analysis outlined in Sect. 2.5) for a case with a negative bias, specifically when WFP is inactive. This negative bias is even more pronounced when WFP is active (due to the momentum extracted from the flow), for which making F3 a useful case to test the performance of a selected FDDA setting. Finally, time frame F4 spans across four days, from 30 January 2023 to 3 February 2023. The goal during this period is to demonstrate the capabilities of the selected FDDA setting
355 for a case with a positive bias, again when WFP is inactive. Additionally, this period also involves significant changes in wind speed data. This is identified using a straightforward SCADA data filtering approach, in which a time period is of interest if the difference of two consecutive wind speed data points (5 minutes apart) is larger than the corresponding standard deviation of 3.93 m s^{-1} . This allows testing the robustness of the selected FDDA setting under rapidly changing wind conditions.

~~In each of the time frames (F1, F2, F3, F4), we consistently perform two baseline simulations~~ are always performed: forecasts
360 without WFP and with WFP. Complementing these, depending on the time frame of interest and its goals. The first simulation, referred to as ‘WFP_off’ in subsequent figures, does not account for the presence of wind farms within the computational domain. The second simulation, labeled ‘WFP’, incorporates the effects of these wind farms via the Fitch WFP. Within time frame F2, we perform numerical experiments of nudging local wind information from either SCADA or LiDAR data source (that is translated into horizontal wind components) an extensive set of 20 numerical experiments to assess the sensitivity of
365 results to varying nudging parameters. The details of all these simulations are listed in Table 2, including their naming, and details on whether WFP is on or off, whether FDDA is performed and if yes, with what properties. In the week-long Frame 1 (this study are elaborated in Sect. 2.5. This helps to identify a preferred (optimal) nudging setting. This setting is then applied to the other case studies F1, F3, F4 (labeled ‘WFP FDDA’). For time frame F1), we aim to improve predictions via hub-height SCADA FDDA (with a radius of influence $R_{xy} = 4$) of wind turbine data with respect to SCADA. This is verified at the two
370 selected subsets (front WTs and waked WTs). The expectation is to thus enhance predictions in time for wind speed, wind direction, and power. Furthermore, in a day-ahead Frame 2 (, we conduct a comparative analysis of four distinct numerical experiments (two baseline simulations and two FDDA configurations). In the case of F3 and F4, we carry out three simulations (two baseline and one with FDDA).

2.5 Insight into optimal FDDA practices: numerical experiments in F2

375 In this section, we describe the sensitivity study conducted during time frame F2), we explore the leverage of having available observations upstream from the Westhinder LiDAR profiler: we assimilate observations at 104.5 height in all numerical

~~experiments. This is accompanied by~~, from 17 February 2022 to 18 February 2022. The primary objective of this study is to gain insight into the optimal practices for FDDA, particularly focusing on varying the nudging strength and radius of influence. The specific values of the nudging parameters used in this study are detailed in Table 3.

380 Within F2, we perform a sensitivity study ~~of the results to the~~ examining the impact of the radius of influence ~~of observational nudging in FDDA: for the Westhinder LiDAR (being 42 further)~~, the FDDA experiments are with ~~and the nudging strength in FDDA~~. The assimilation of upwind LiDAR data is performed for 15 numerical experiments (including one cyclic configuration) in which we vary the radius of influence ~~of $R_{xy} = 10, 20, \text{ and } 30$~~ , whereas for the cases of SCADA nudging, R_{xy} and the nudging strength G_q . The assimilation of SCADA is performed for 3 cases (in which we vary only R_{xy}). For the SCADA nudging cases (labeled S01-S03), we test values of $R_{xy} = 2, 4 \text{ and } 10 \text{ km}$ ~~are chosen. Additionally, for the case of FDDA of LiDAR with~~. For the WHi LiDAR nudging cases (labeled L01-L14 and LC04), we assimilate upwind observations at a height of 104.5 m. The tested values of the radius of influence are $R_{xy} = 10, 20, 30, 40, 50, \text{ and } 60 \text{ km}$. We remind that the WHi LiDAR is situated 47 km further from the wind farm sites, and that the key aspect is to leverage these upwind observations. In addition, for the LiDAR FDDA cases with a radius of influence ~~$r = R_{xy} = 20 R_{xy}$ of 20 km~~ (as in e.g. Cheng et al. (2017)), ~~three as well as 30 km, we consider five values of nudging strength G_q are considered: $6 \times 10^{-4} \text{ s}^{-1}$ (a typical default value, e.g. in Cheng et al. (2017)), a five-times-stronger value values of $3 \times 10^{-3} \text{ s}^{-1}$, and lastly, ten-times stronger $G_q = 6 \times 10^{-3} \text{ s}^{-1}$, $9 \times 10^{-3} \text{ s}^{-1}$. After confirming the leverage of the upstream (LiDAR) observations, we propose a simple yet realistic forecasting routine where FDDA of upstream, and the strongest value of $3 \times 10^{-2} \text{ s}^{-1}$. This yields 10 numerical experiments. Furthermore, for the nudging strength of $6 \times 10^{-3} \text{ s}^{-1}$, we consider 4 additional cases with radius of influence~~ of 10, 40, 50, and 60 km.

395 Finally, we propose a practical routine for hour-ahead predictions in which FDDA of upwind LiDAR data is performed in a ~~cyclical manner: for a certain amount of time (in this case, one hour window is selected)~~, upstream-cyclic manner. In this routine (labeled 'LC04' in Table 3 and in subsequent figures) upwind LiDAR data is assimilated for one hour and its effect is ~~propagating propagates~~ as the simulation is running. After this one hour has passed, DA ends runs. Once this one-hour window ~~elapses, the DA ends~~, and the model continues to run without ~~any further data assimilation, leading to improvements in forecasts further assimilation. This leads to prediction improvements~~ solely due to the ~~propagating wind information downstream that is downwind propagation of advanced wind information~~ induced by the FDDA effect. ~~For Given~~ the distance of approximately 42 ~~47 km from the Westhinder LiDAR to the Belgian-Dutch cluster, this implies 20-70 minutes of advection time and an advection time of 20-70 minutes and a~~ lasting effect of the DA after its end ~~(in this case, one hour)~~. This procedure can be ~~performed~~ ~~repeated~~ as many times as desired ~~(, using WRF restart files to ensure the model has spin-up) and improvements~~. Every restart should be considered as a separate forecast simulation initiated at the time of the completion of LiDAR data collection (ideally available in real-time), so in this view, no future data is assimilated in the model. Improvements can be achieved in any area of interest, ~~as long as provided~~ the data source is ~~upstream: in upwind~~. In this configuration, ~~this is the case~~ when the wind is from ~~the~~ South-West. ~~All these different numerical experiments yield 3 cases for F1, and 11 cases for F2. All simulations for~~ ~~F1 and F2 with their corresponding names are listed in Table 2.~~

Table 3. All simulations performed within the F2 time frame, with varied nudging strength G_q and horizontal radius of influence R_{xy} . S01-03 denote three numerical experiments in which SCADA is assimilated, whereas L01-L14 are simulations with only upwind LiDAR assimilation. In all of these simulations, the assimilation time window over which each observation point is used in the nudging algorithm is $\tau = 0.6667$ hours (40 minutes). Finally, LC04 is the artificial cyclic configuration for hour-ahead predictions, in which $\tau = 0.16667$ hours (10 minutes).

	$G_q = 6 \times 10^{-4} \text{ s}^{-1}$	$G_q = 3 \times 10^{-3} \text{ s}^{-1}$	$G_q = 6 \times 10^{-3} \text{ s}^{-1}$	$G_q = 9 \times 10^{-3} \text{ s}^{-1}$	$G_q = 3 \times 10^{-2} \text{ s}^{-1}$
$R_{xy} = 2 \text{ km}$	S01				
$R_{xy} = 4 \text{ km}$	S02				
$R_{xy} = 10 \text{ km}$	S03				
$R_{xy} = 10 \text{ km}$	L01				
$R_{xy} = 20 \text{ km}$	L02	L03	L04, LC04	L05	L06
$R_{xy} = 30 \text{ km}$	L07	L08	L09	L10	L11
$R_{xy} = 40 \text{ km}$	L12				
$R_{xy} = 50 \text{ km}$	L13				
$R_{xy} = 60 \text{ km}$	L14				

~~Timeline of the storms. The focus at first is on enhancing predictions via FDDA of SCADA during all three storms (F1, week-ahead). Then — on performing further numerical experiments over one day (F2, day-ahead), aiming to gain insight into favorable FDDA practices.~~

3 Results and ~~Discussion~~discussion

415 This section is dedicated to comparing the results from the simulations at the five locations of interest (the upstream upwind Belgian WHi LiDAR; the “Front WTs” and “Waked WTs” Front WTs and Waked WTs at the selected Belgian wind farm; and finally, the two Dutch LiDARs, EPL and LEG). ~~To evaluate simulation performances, we utilize traditional metrics and compare the mean absolute error (MAE, Lydia et al. (2014)) of the different scenarios with respect to the corresponding local observations offshore. MAE is a common evaluation criteria of wind forecasting, as it reflects the overall level of errors~~
 420 ~~(Yang et al., 2021).~~ In Sect. 3.1, we discuss the results from the sensitivity study to nudging parameters in F2, and we identify optimal FDDA configurations. These configurations are then applied to F1, F3, and F4, in Sect. 3.2

3.1 ~~Forecasting with WFP, and enhancing predictions via~~ Results from the numerical experiments in F2 on FDDA of SCADA for week-ahead simulationspractices

~~Figure 5 illustrates results for F1 (week-ahead) with and without the presence of~~ The focus is on the day-long case of 17
 425 February 2022 (F2 in Table 2), with the wind turbines in the computational domain. It showcases the importance of WFP in WRF by displaying snapshots of wind fields for three arbitrary time slots during this period of interest in February 2022. The

wind directions for the three snapshots in Fig. 5 are from South-West (top), South (middle), and West (bottom). Snapshots of wind speed fields (\bar{v}) for three different time instances within F1. On the left, results with active WFP show that energy is indeed extracted from the flow. The middle fields are from the simulation without WFP. On the right, the difference in wind speed fields with and without WFP is shown.

For the week-long F1, the time series at the location of the “Waked WTs” are shown in Fig. 6 (both for the cases ‘F1, WFP’ (a run with active WFP) and ‘F1, WFP FDDA S1’ (a run with active WFP and with FDDA)). For more details on these runs, see Table 2). The wind speed values are normalized by cutoff speed. The power is also normalized by the rated values. The forecast using WFP captures well all three storms in F1, as well as swift wind direction changes, especially before Storm Eunice, and before and during Storm Franklin. In order to enhance the modeling during the three extreme events, we perform FDDA of SCADA data every goal to study the sensitivity effects of varying the radius of influence R_{xy} and the nudging strength G_q of FDDA, while nudging either LiDAR or SCADA data every 10 minutes for the whole duration of F1, which provides further improved predictions of wind speed and wind directions, as indicated by the reduced MAE values for the case ‘F1, WFP FDDA S1’ in Fig. 6.

To evaluate the simulation performances of the different scenarios in the five locations of interest, we present MAEs summarized in Fig. 7, for all three different runs (without WFP, with WFP, and with FDDA of SCADA only) at each location (WHi LiDAR, Front WT, Waked WT, EPL and LEG LiDARs). The predictions at the two wind turbine locations are compared to SCADA data at hub height minutes. As mentioned before, Table 3 summarizes all 18 cases of numerical experiments within F2: nudging SCADA with different radius of influence, and nudging LiDAR with different parameters. We remind that for the FDDA of a LiDAR measurement point at 104.5 m, six values for the radius of influence R_{xy} were tested (10 km, 20 km, 30 km, whereas the predictions at the three LiDARs are compared to observations at corresponding heights listed in the caption of Fig. 7. Moreover, Fig. 7 emphasizes that WFP helps improve the wind speed, but not the wind direction, whereas further introducing FDDA of SCADA improves both wind speed and wind direction, especially at the wind farm location. At the LiDARs (EPL and LEG, approximately 63–40 km downstream from the, 50 km, and 60 km), whereas for SCADA FDDA – 2 km, 4 km, and 10 km were considered. FDDA of solely upwind observations (in this case, from the Westhinder LiDAR) allows for advanced wind information to propagate to the wind farms in the Belgian-Dutch cluster for (an order of) 20–70 minutes in advance.

The effect of different radius of influence and nudging strength can be seen in Fig. 4. This figure shows the difference with and without FDDA of upwind LiDAR for three different cases:

- L02 (Fig. 4(a)) with $R_{xy} = 20$ km and with the default (and lowest) nudging strength value $G_q = 6 \times 10^{-4} \text{ s}^{-1}$, results remain almost intact. FDDA of in-situ observations such as SCADA provides prediction enhancements which are useful for reanalysis of various events and detailed wind resource assessment, especially if performed for long periods of time
- L04 (Fig. 4(b)) with $R_{xy} = 20$ km and with a ten times larger nudging strength $G_q = 6 \times 10^{-3} \text{ s}^{-1}$,
- L14 (Fig. 4(c)) with $R_{xy} = 60$ km and $G_q = 6 \times 10^{-3} \text{ s}^{-1}$.

The simulations

Wind speed fields with and without FDDA [m/s]

Difference in wind speed fields [m/s]
with and without FDDA of LiDAR

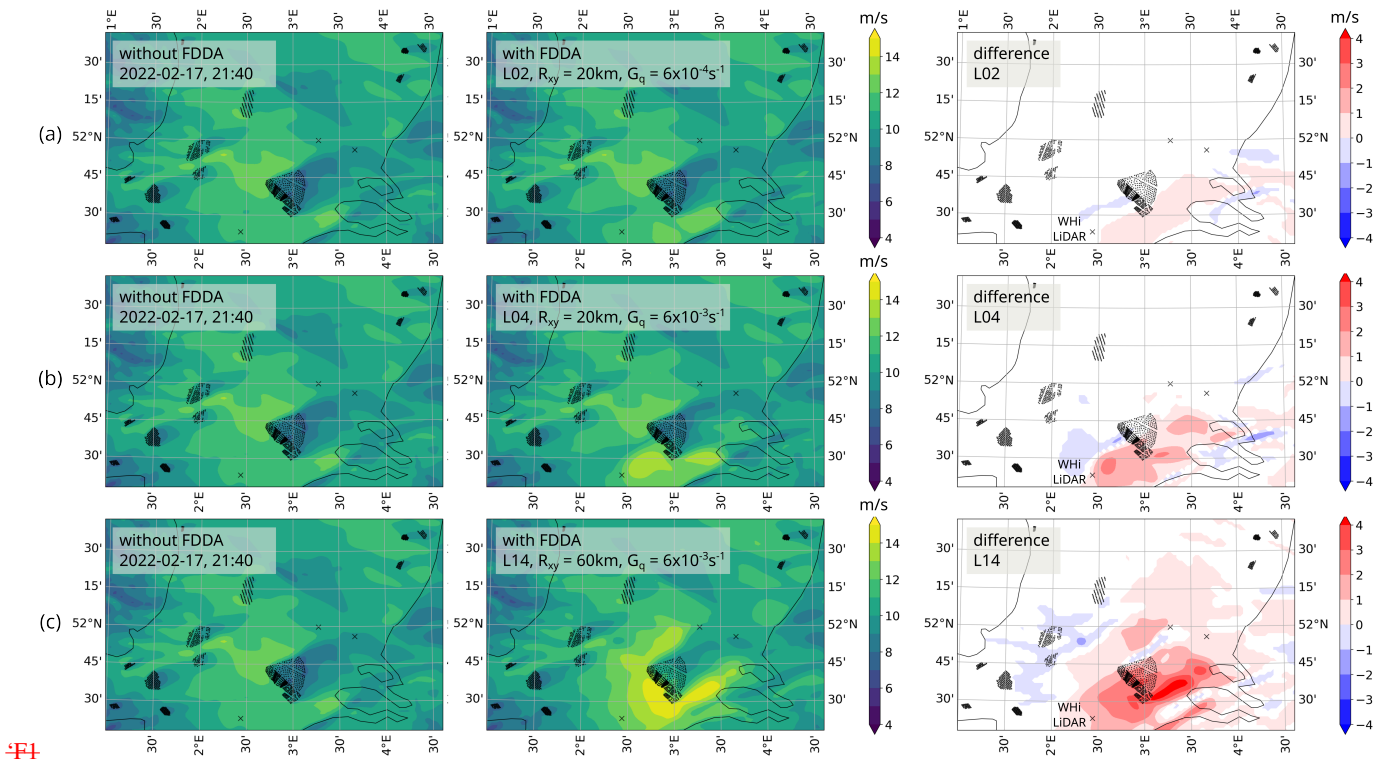


Figure 4. Snapshots of wind speed fields (m s^{-1}) on 17 February 21:40 UTC, of simulations L02 (a), L04 (b), and L14 (c). In the left columns, the results are without assimilation, in the middle columns – with FDDA, and finally in the right columns the differences between the two are shown.

460 Figure 4 shows the importance of the two nudging parameters R_{xy} and G_q . Varying their values implies resulting wind field modifications. In turn, these changes need to be compensated to preserve conservation laws, which is why we observe both positive and negative changes of wind speed values in the difference fields of Fig. 4.

To explore the performance of the numerical experiments in F2, we compute the MAEs for each measurement height with respect to the WHi LiDAR profile, at the WHi LiDAR location of assimilation (for verification purposes). This is the averaged profile in time frame F2. In Fig. 5, we visualize these MAEs for all different simulations (listed in x-axis) in which LiDAR data is assimilated (see Table 3), as well as the two baseline simulations: a simulation with WFP only (a control run with no FDDA), and a simulation without any WFP. It is indeed expected that MAEs are always reduced at the assimilation location WHi when LiDAR FDDA is performed there. Although the assimilated LiDAR data point is positioned at a measurement height of 104.5 m, we observe enhancements in the entire profile, evident in both wind speed (Fig. 5(a)) and wind direction (Fig. 5(b)). This widespread improvement in height is attributed to the default setting of the vertical radius of influence in FDDA, which spans

470

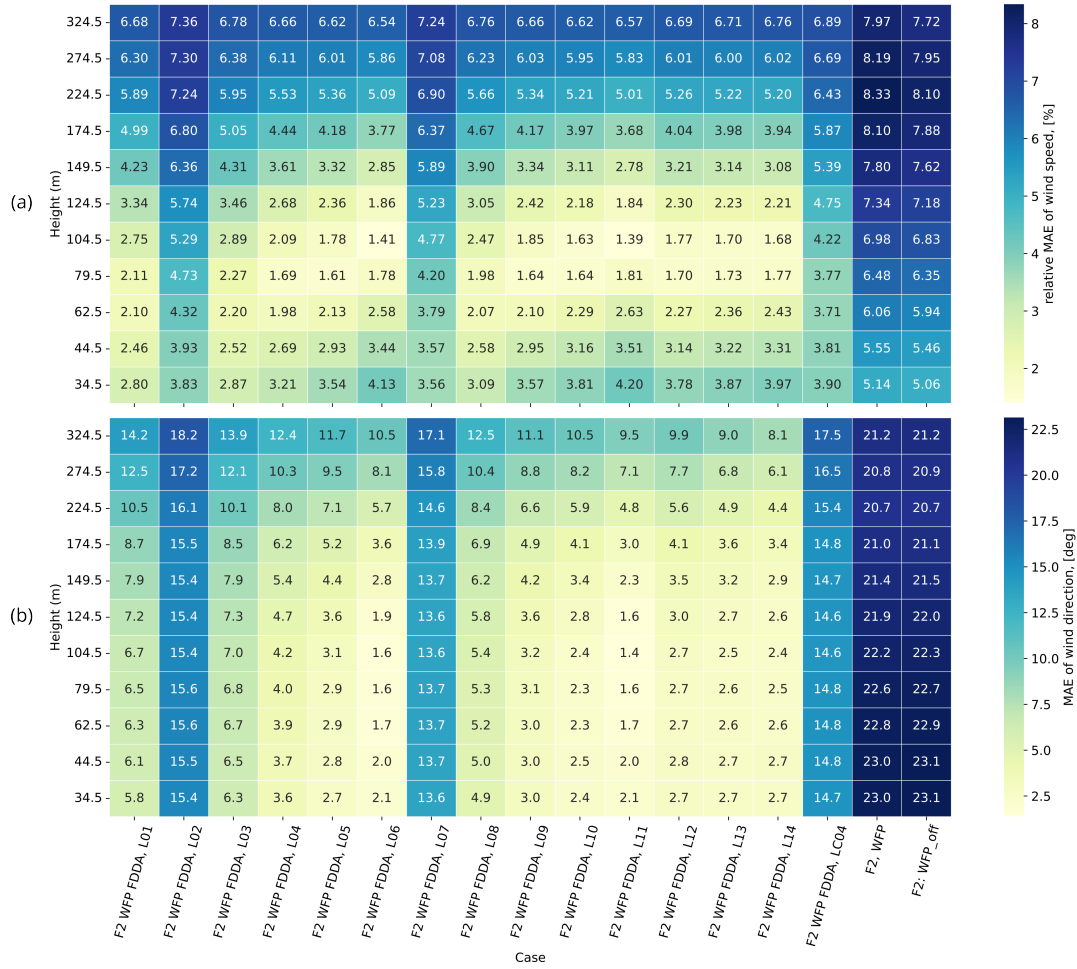


Figure 5. MAEs at hub height: results at the waked-WTs-WHi assimilation location during, computed for each measurement height with respect to the three storms mean profiles from the Westhinder LiDAR observations for simulations in F2.

across all model levels. Hence, the absence of vertical constraints in this influence helps avoid the formation of unusual profiles. Consequently, the assimilation of a LiDAR data point at a single height leads to improvements observed throughout the entire profile. In terms of horizontal influence, improvements are especially pronounced when the horizontal radius of influence R_{xy} and the nudging strength G_q are set to higher values (as seen for example in L06, WFP and F1L11). However, when the default value is used for G_q (as in L02, WFP-FDDA-S1L07) the reduction in MAEs is not as substantial. It is worth remarking also the improvements in the LiDAR cyclic FDDA routine, case 'F2, WFP FDDA, LC04' when assimilating SCADA.

Mean absolute errors (MAEs) computed for each run at five different locations. The errors are estimated with respect to local observations: three LiDAR profilers (WHi at 104.5, EPL at 116, LEG at 115) and two subsets of WTs providing SCADA at hub height.

In this section, we perform day-ahead predictions (For a full evaluation and determination of optimal FDDA practices, we analyze all experiments within F2 in Fig. 4) and study the effect of radius of influence of FDDA while nudging either LiDAR or SCADA data. Table 2 can be used as reference as it summarizes all 11 cases of numerical experiments within, detailed in Table 3, by presenting wind speed RMSEs and biases in Fig. 6. Additional error data on wind direction and power is shown in Appendix B. Figure 6 illustrates the numerical results at five locations, benchmarked against local observations. For enhanced clarity, the cells which coincide with an assimilation location have been crossed out, directing the attention to improvements at more distant locations. It is particularly encouraging that the FDDA of the WHi LiDAR point (at a height of 104.5 m) leads to improvements in results 47 km downwind at turbine sites, outperforming the baseline simulations without FDDA ('F2: with and without WFP, nudging LiDAR with different parameters, WFP_off' and 'F2, WFP'). When utilizing the default nudging strength value of $6 \times 10^{-4} \text{ s}^{-1}$, relatively small error reductions are observed downwind at the turbine locations (Front and Waked WTs) in L02 and nudging SCADA with different L07, with L07 outperforming L02 due to its greater horizontal radius of influence. For the FDDA of a LiDAR data point at 104.5, three values for the radius of influence R_{xy} were tested (10 (30 km). Similarly, among other pairs with equal nudging strength but differing horizontal radii of influence, L08 surpasses L03, 20 L10 outperforms L05, and L11 excels over L06 due to the greater radius value. The cases L01, L04, L09, L12, L13, L14 share a nudging strength of $6 \times 10^{-3} \text{ s}^{-1}$, with horizontal radii of influence spanning from 10 km as in Cheng et al. (2017), for L01 to 60 km for L14. Interestingly, L09 that has $R_{xy} = 30 \text{ km}$, demonstrates the most substantial error reduction in this group: increasing the radius beyond 40 km leads to increased biases, as shown in Fig. 6(b). Thus, L04 and L09 (with horizontal radii of 20 and 30 km, respectively) become apparent balanced configurations. Furthermore, while examining varied nudging strengths with a fixed radius R_{xy} of 20 km (L02, L03, whereas for SCADA FDDA — 2 L04, L05, L06), and of 30 km (L07, L08, 4 L09, L10, L11), we find consistent RMSE and bias improvements as nudging strength is increased while $R_{xy} = 20 \text{ km}$. Yet, at 30 km biases worsen despite (inconsistent) RMSE gains. Thus, $R_{xy} = 20 \text{ km}$ is identified as an optimal choice for a horizontal radius of influence. Among L04, L05 and 4 L06, no significant differences are present, which leads to the selection of L04 as the preferred FDDA setting. Therefore, the parameters of L04 and/or L06 are applied in Sect. 3.2 for F1, F3, F4, as well as in a proposed cyclic routine for F2 in the current section. Finally in Fig. 6, at the more distant EPL and LEG LiDAR comparison locations (approximately 110 km were considered. The configurations offn these 11 cases are detailed in Table 2. FDDA of solely upstream observations (in this case, from the Westhinder LiDAR) has strong advantages, especially being computationally inexpensive and allowing for wind information to propagate to the wind farms in the Belgian-Dutch cluster for (an order of) 20-70 minutes in advance away from the assimilation at WHi LiDAR), wind speed fields remain largely unaffected, except when the horizontal radius of influence reaches 50 or 60 km.

510 Figure 8 shows predictions in the “Waked WTs”

Figure 7 shows results in the Waked WTs location for three variables: wind speed, wind direction, and power. The wind speed values are again normalized by cutoff speed (31 m s^{-1}). The power is also normalized by a typical rated value (8.4 MW). These results are obtained when nudging only LiDAR upstream. The predictions WHi LiDAR upwind. The results are

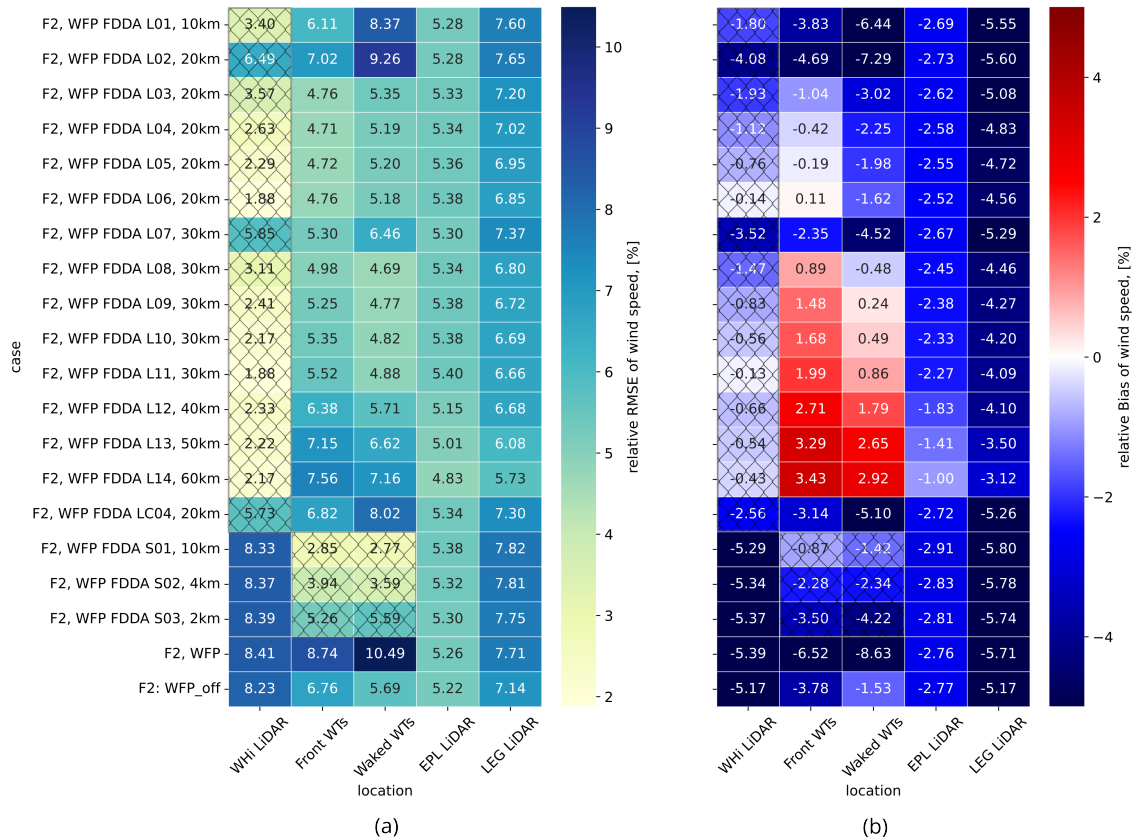


Figure 6. Color maps of MAE (a) and bias (b) for wind speed for the different simulations computed at the five locations with respect to the corresponding observations: WHi at 104.5 m, EPL at 116 m, LEG at 115 m, and Front and Waked WTs at hub height. Results at assimilation locations are marked with crossed-out cells.

515 compared to SCADA data ~~downstream~~ (the average of the observations of the selected subset of turbines in the wake) ~~downwind~~ at farm sites. When performing FDDA of LiDAR, improvements in ~~predictions downstream results downstream~~ (at the ~~waked~~ Waked WTs) are evident based on the reduced MAEs in Fig. 8 for the legends of Fig. 7 for (a) wind speed, (b) wind direction and (c) power. Although the WHi LiDAR is located ~~42-47~~ km ~~upstream away~~ from the wind farm of interest, the wind direction is favorable and from mostly South-West and allows the nudged information to propagate towards the zone of interest (at the Belgian wind farms).

520 Having ~~upstream-upwind~~ observations proves to be especially useful based on the results so far. ~~Therefore, we will now explore a cyclic configuration of FDDA as a forecasting routine.~~ Overall, the use of nudging shows a significant improvement compared to simulations without it. This methodology can be used as long as local observations are available, but in order to utilize this in ~~forecasting mode~~ a forecasting setting, it is required to understand the behaviour of the FDDA method when the data stops being fed into the simulation. Therefore, to expose the reach of this method, we ~~will now~~ explore a cyclic

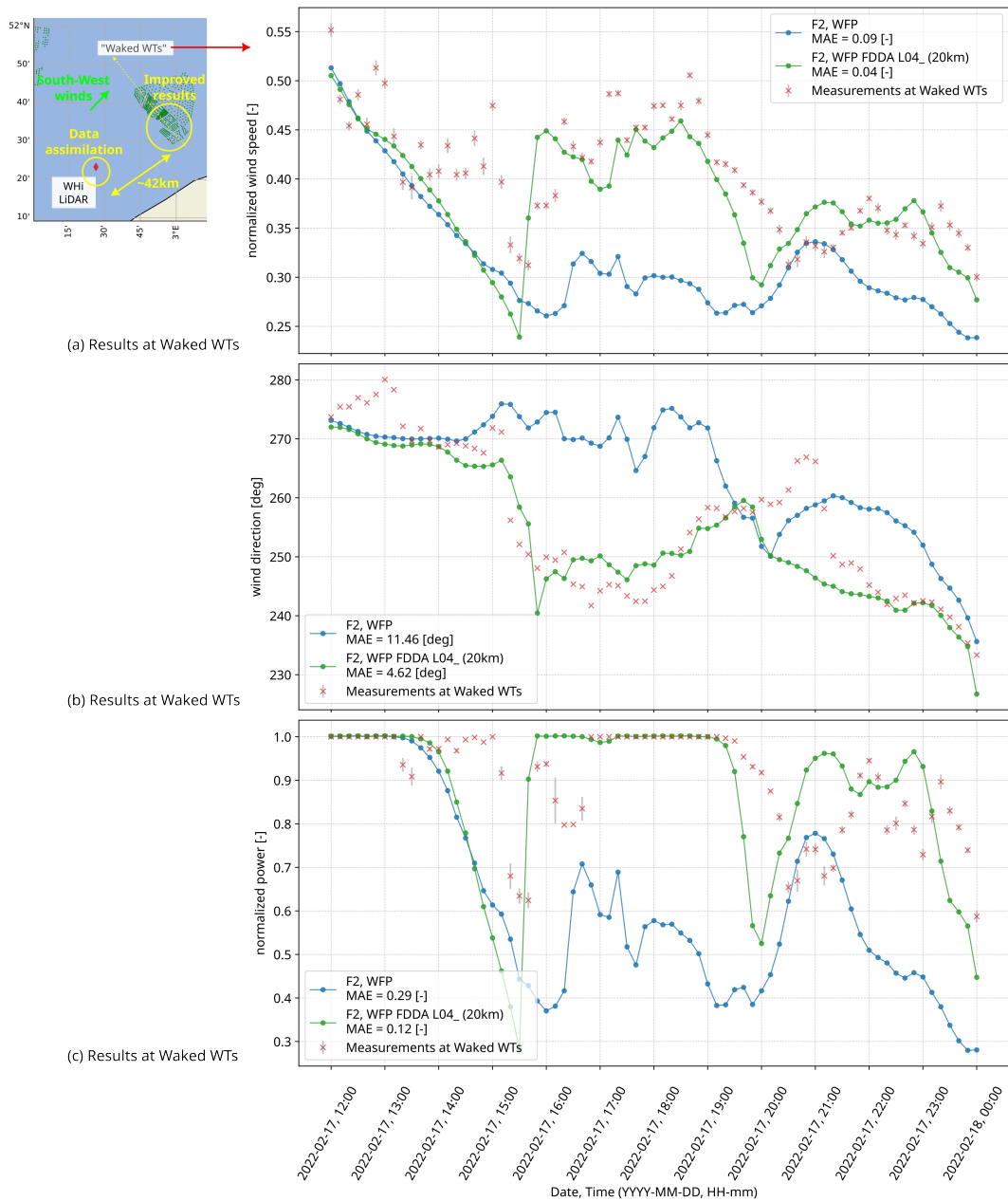


Figure 7. Predictions from the simulations Simulation results with and without upstream assimilating upwind WHi LiDAR ('F2, WFP FDDA L04') that are compared to SCADA data downstream from waked WTs. Wind speed (topa), wind direction (middleb), and power (bottomc). Improvements when performing FDDA are highlighted by displaying the MAE values for each variable in the legends. The grey error bars indicate the standard error (available from SCADA only for wind speed and power).

525 numerical experiment of FDDA ~~for hour-ahead predictions. Ideally, real-time data access would be a requirement.~~ We nudge
the simulation variables closer to observations ~~in a similar manner similarly~~ as in the previous sections, but only during short
~~(one hour)~~ periods of time (nudging windows, abbreviated as ‘N-WNW’). ~~Note that these nudging windows are different from~~
~~the assimilation time window τ , which defines the amount of time for which a single observation is considered in the nudging~~
~~algorithm (τ is responsible for the temporal weighing function w_t in W_g of the algorithm).~~ The assimilation is done again at
530 the WHi LiDAR ~~upstream-upwind~~ with a nudging radius of influence of 20 km, ~~as in Cheng et al. (2017). Figure 9 and with the~~
~~nudging strength of L04.~~ Figure 8(a) shows the wind speed ~~predictions simulation results for F2 (17 February 2022)~~ at the WHi
LiDAR ~~(top)~~ while assimilating wind data at a height of 104.5 m in four nudging windows, ~~each with a duration of 1 hour each.~~
The first nudging window (N-W1NW1) is from 12:00 h to 13:00 h followed by a forecasting window (FC-W1FCW1) of 2
hours; the second ~~one (N-W2 nudging window (NW2))~~ is from 15:00 h to 16:00h, and so on. ~~The assimilation window τ during~~
535 ~~which observations are considered by the model is also indicated in the figure (only in N-W3 for illustrative purposes)~~ ~~Each~~
~~new nudging window begins with a restart of the simulation.~~ As expected, ~~we observe that at the nudging location,~~ wind
speed gets closer to the ~~LiDAR~~ observations within the nudging time. ~~We However, we~~ also observe in Fig. 9 ~~(bottom)~~8(b)
that those quantities still follow better the ~~observations taken downstream SCADA observations downwind,~~ even after the end
of ~~nudging window the nudging window (in the first hour of all forecasting windows).~~ This is explained by the ~~location of~~
540 ~~the prominently positioned LiDAR~~ observations with respect to the wind farm ~~. The WHi LiDAR is prominently positioned~~
~~with respect to from~~ the Belgian-Dutch cluster. This ~~position~~ allows for the ~~quantities being assimilated assimilated quantities~~
~~(during the nudging window) to be propagated downwind to be advected downstream to the wind farm, therefore their values~~
~~. This advection time is of the order of one hour, and therefore the wind variables~~ at the wind farm are still influenced after
the assimilation has stopped. ~~After the advection time, the simulation resumes back to the reference run with no FDDA. This~~
545 ~~is especially noticeable 40-50 minutes after the end of a N-W due to τ being set at approximately 40 minutes.~~ These lead to
improved ~~forecasts downstream model output downwind~~ at the waked wind turbines, as indicated ~~for example~~ by the reduced
MAE values in ~~in Fig. 9 (bottom) . The difference with and without FDDA of upstream LiDAR for the case ‘F2, WFP FDDA,~~
~~L6’ can be seen in Fig. 10 for a certain snapshot during this simulation. Fig. 8 (b) for normalized wind speed, from 0.09 to~~
~~0.06.~~

550 We thus demonstrated a ~~eyeling cyclic~~ routine with four nudging windows to showcase ~~this effect. With this method for using~~
~~observations to improve predictions within the hourly range, a the potential for hour-ahead improved predictions.~~ A LiDAR
that is strategically situated (such as in all of these study cases) can become an essential asset for wind farm decision-making,
especially for extreme weather events like a storm, or a frontal passage. Due to the enormous impact that ~~this these events~~
might have for wind farm operators, it can be expected that the use of this method will motivate more measurement campaigns
555 offshore, with real-time access. The main limitation of this strategy is when the flow direction is not ~~in its predominant direction,~~
~~where from South-West, because~~ we would no longer have LiDAR observations upstream ~~with respect to this direction;~~ in that
case, the wind farm is no longer ~~downstream downwind~~ of the nudged quantity, and therefore remains (almost) unaffected.

A snapshot of wind speed fields (-) on 17 February 21:40 UTC +1, of ‘F2, WFP FDDA, L6’ (left) and ‘F2, WFP’ (without
FDDA) (center), as well as the difference between the two (right).

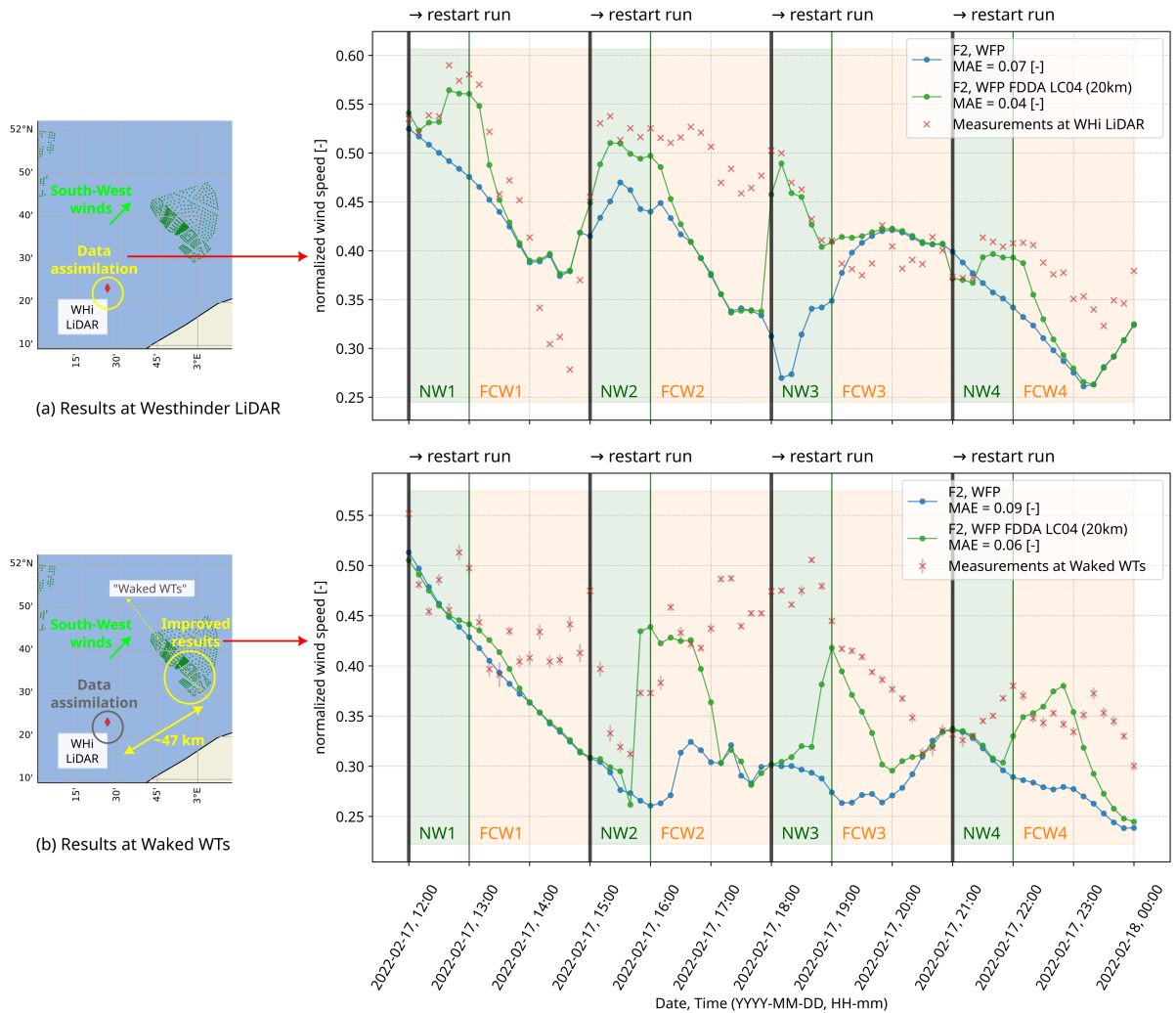


Figure 8. Wind speed Artificial cyclic routine 'F2, WFP FDDA LC04' for hour-ahead predictions: wind speed results at the Westhinder platform (a), compared to the assimilated LiDAR data (top), while assimilating wind data at a height of 104.5 m in four nudging windows (NW1-4 denoted as NW1-4, one hour each). Information is adveected downstream-propagated downwind to the location of the waked WT's, and the results are compared to SCADA (bottom). Forecasting windows have a 2-hour length and are denoted as FCW1-4 FCW1-4. MAE values are reduced for The grey error bars indicate the ease of cyclic nudging in 'F2, WFP FDDA L6' as compared to when no FDDA is performed standard error (in 'F2, WFP' available from SCADA only for wind speed and power).

560 3.2 Results for cases with different weather conditions using WFP and FDDA

To further assess how the F2 day-ahead simulations perform, we compute the MAEs in height with respect to the WHi LiDAR profiles. In Fig. 11, we visualize the MAEs in height for the different simulations (listed in x-axis) that are using LiDAR data

(see Table 2). The height of the assimilated LiDAR point is solely at 104.5, yet improvements with respect to observations are perceived along the whole profile. A vertical smoothing in wind speed profiles is expressed in this figure which ensures the smooth transition between simulation and observation. Furthermore, the MAEs are reduced. We discuss results obtained for time frames from Table 2 (F1, F3, and F4) using the findings from the sensitivity study to nudging parameters in Sect. 3.1. Let us first illustrate results with and without the presence of wind turbines in the computational domain in Fig. 9 for F1. This figure displays snapshots of wind fields for three arbitrary time slots during this period of interest in February 2022. The wind directions for the three snapshots in Fig. 9 are from South-West (a), South (b), and West (c). Significant velocity deficits are observed in all cases, as well as inter-farm interactions. For the whole duration of the four-day long time frame F1, simulation results at the Waked WTs location are shown in Fig. 10. These results are both for the cases where LiDAR FDDA is performed. The case ‘F2, WFPFDDA, L1’, that has a typical nudging strength G_q , shows reduction of MAEs of about 1.3–1.4 times for both wind speed and wind direction at 104.5. ‘F1, WFP’ (with active WFP) and ‘F1, WFP FDDA L04’ (with active WFP and with FDDA of LiDAR located further upwind). The wind speed values are normalized by a representative cut-out speed (31 m). Improvements are especially pronounced when R_{xy} and G_q have higher values. For example, for the case with no data assimilation ‘F2, WFP’, the MAE of normalized wind speed at the height of 104.5 is 0.070, whereas when assimilating LiDAR with $R_{xy} = 20$ in ‘F2s⁻¹). We remind that the details on nudging values for L04 are in Table 3. The results using WFP captures well the storms in F1, as well as swift wind direction changes, especially before and during Storm Franklin (19 February 2022 at 18:00, 20 February 2022 at 21:00). In order to further enhance the model output during the three extreme events, we perform FDDA of upwind WHi LiDAR data every 10 minutes for the whole duration of F1, which improves significantly the results of wind speed and wind directions, as indicated by the reduced MAE values for the case ‘F1, WFP FDDA, L3’, the MAE is reduced to 0.021 (about 3.3 times). Similarly for these two cases, the MAE of wind direction is reduced about 5.2 times. It is worth remarking also the improvements in the cycling FDDA routine, case ‘F2, WFP FDDA, L6’, are expressed as MAE reduction for wind speed of about 1.9 times, and for wind direction of about 2.3 times.’ (L04) in Fig. 10.

585 In height: MAEs computed with respect to the LiDAR observations at the Westhinder platform

Figure ?? compares the MAEs from results at the five locations (with respect to the corresponding local datasets) for the day-ahead predictions for all the cases described in Table 2, namely when not performing any nudging ‘F2, WFP_off’ and ‘F2, WFP’, when nudging only LiDAR data ‘F2, WFPFDDA, L1-6’s, and when nudging only SCADA ‘F2, WFP FDDA. To evaluate the performance of the different scenarios in wind speed and wind direction results, we present their errors, summarized in Fig. 11. This involves time frames F1, F3, F4, with their corresponding options (without WFP, S1-3’s, all of which have their parameters detailed in Table 2. It is particularly encouraging that performing FDDA of a single LiDAR point (at 104.5) upstream from the wind farm zone can lead to improvements in predictions downstream at the wind turbines locations, as seen from the first six rows in Fig. ??, especially in comparison to the last two rows (corresponding to the baseline runs ‘F2: WFP_off’ and ‘F2, WFP’). Performing FDDA of SCADA also enhances (locally) the predictions (the three rows corresponding to ‘F2, WFP FDDA, S1-3’ with the three different radius of influence 10, 4, and 2. Further downstream at the EPL and LEG LiDARs, the fields are almost unaffected, similarly to the week-long case. Additionally, and with FDDA) at the Waked WTs location. The FDDA configuration used is also specified (L04 or L06 from Table 3, which is supported by the

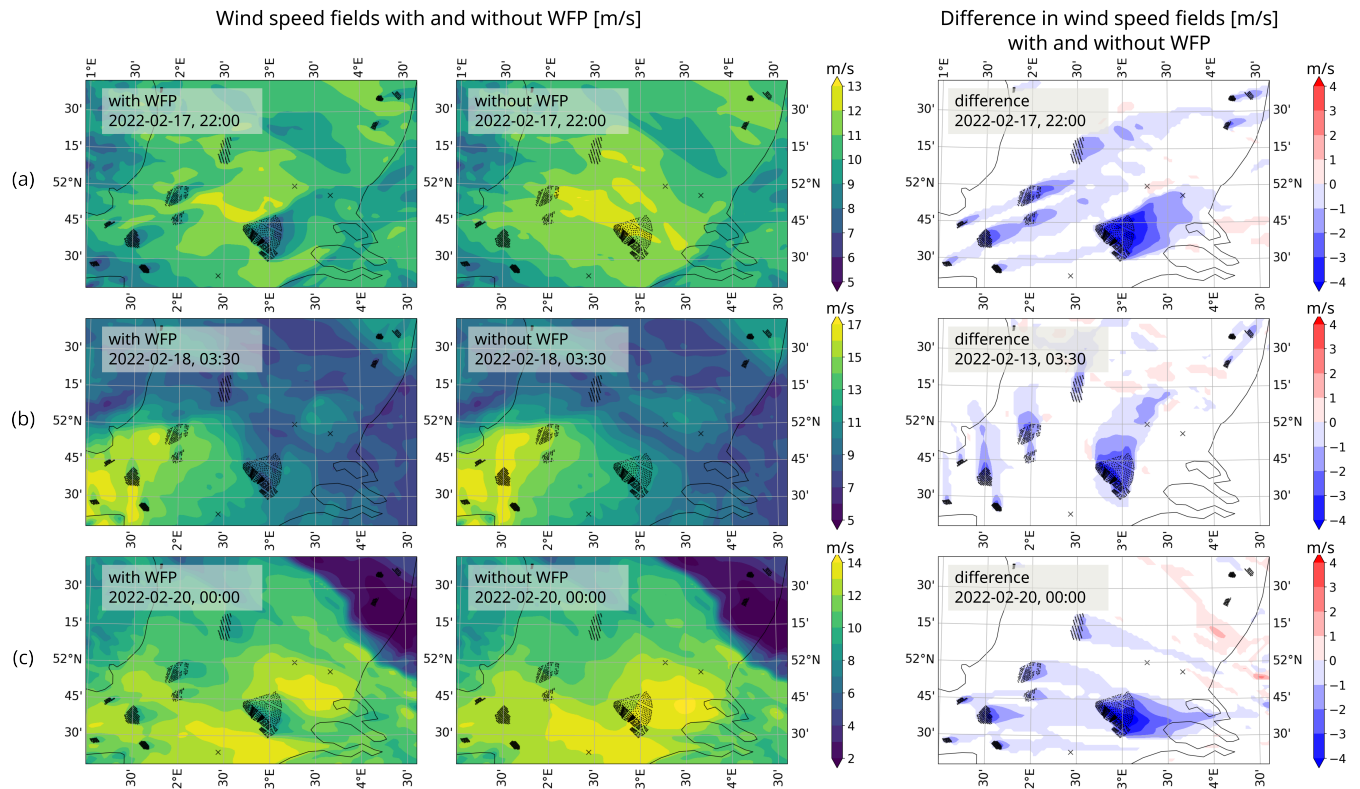


Figure 9. Color maps Snapshots of MAEs for wind speed and wind direction fields (m s^{-1}) for the three different simulations computed at time instances within F1 (a, b, c). On the five locations left column, results with respect to active WFP show that energy is indeed extracted from the corresponding observations: WHI at 104.5 flow. The middle fields are from the simulation without WFP. On the right, EPL at 116, LEG at 115, the difference in wind speed fields with and Front and Waked WTs at hub height without WFP is shown.

sensitivity study in Sect. 3.1). Moreover, Fig. 11(a) emphasizes that activating WFP helps improve wind speed, but not wind direction. This is the case for F1 and F4, except if the relative bias of wind speed with respect to SCADA data is already negative when WFP is inactive. In that case, the wind power extraction will further bring this bias to more negative values, as it is the case for F3 in Fig. ??, power improvements due to FDDA are also significant and are summarized for all cases that have an active WFP. For normalized power at the Front WTs, the cases of upwind LiDAR data assimilation ‘F2, WFP FDDA, L1-6’ show a reduced MAE by 1.8–2.6 times in comparison to ‘F2, WFP’ (without DA), whereas for the cases of SCADA ‘F2, WFP FDDA, S1-3’ this reduction is of the order of 3.2–4.7 times due to the available in-situ observations 11(c). Therefore, for frame F3, activating WFP does not improve MAE of wind speed as shown in Fig. 11(a). Activating WFP has almost no impact on wind direction MAEs (Fig. 11(b)) and biases (Fig. 11(d)). However, the introduction of the upwind LiDAR FDDA improves both wind speed and wind direction. FDDA of such observations provides enhanced results that are useful for weather reanalysis, as well as for detailed wind resource assessment.

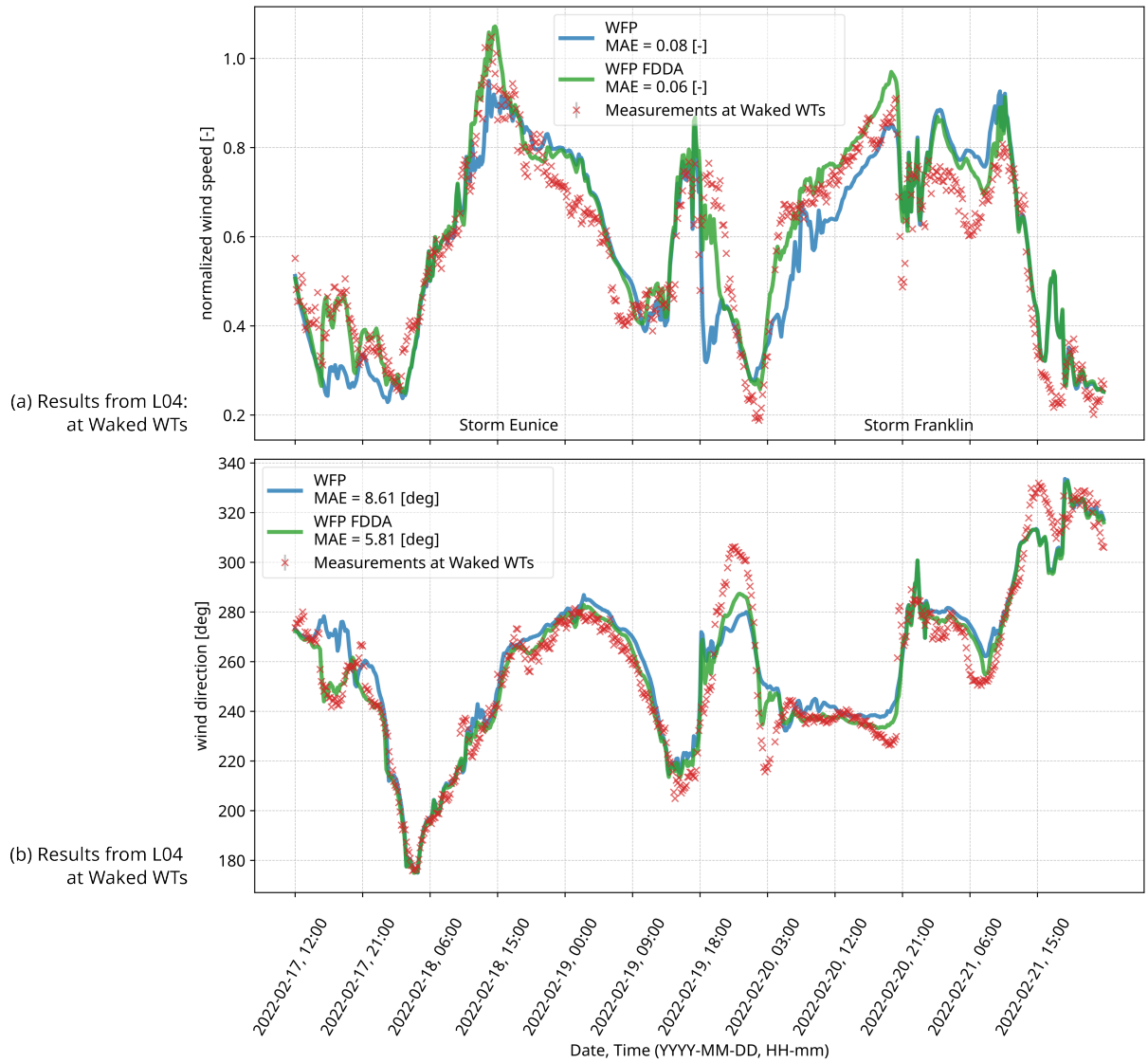


Figure 10. MAEs for normalized power for the different The simulations that have an active ‘F1, WFP’ and ‘F1, computed WFP FDDA’ (L04) when assimilating (upwind) LiDAR data, 47 km away: results at the two wind farm locations (front and waked Waked WTs)location during the Eunice and Franklin storms. UTC timezone.

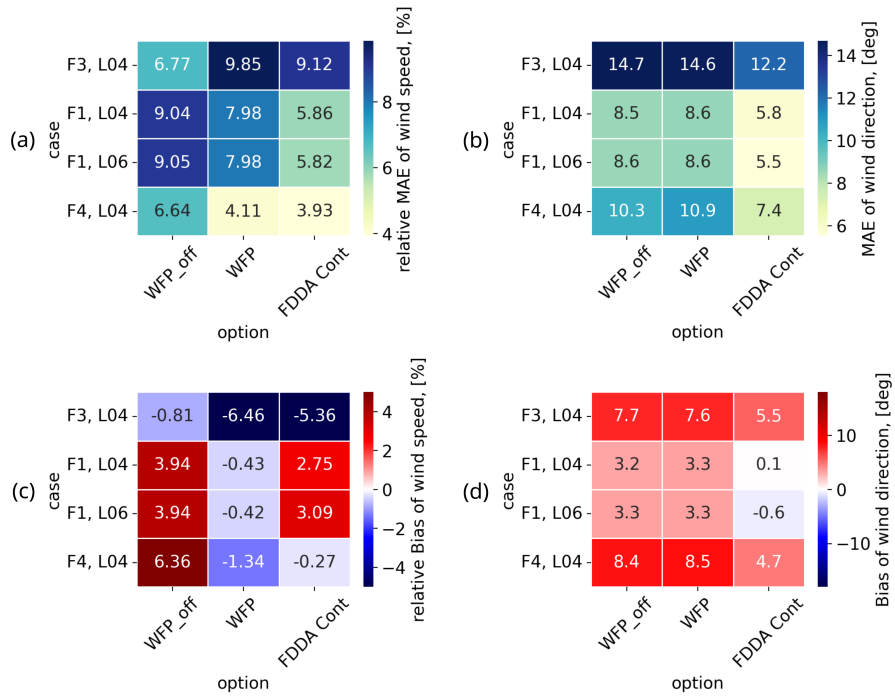


Figure 11. Mean absolute errors (MAEs) of wind speed (a) and of wind direction (b), computed for each case at the Waked WT's location. Bias of wind speed (c) and of wind direction (d) for each case at the Waked WT's location. Data is assimilated only at WHi LiDAR.

4 Conclusions

610 This study demonstrated the usefulness of assimilating local offshore observations (such as ~~from SCADA or~~ LiDAR) in NWP models (in this case, via ~~FDDA the~~ FDDA algorithm in the Advanced Research WRF model) to improve ~~predictions of wind direction, wind speed simulation results of wind speed, wind direction~~ and, consequently, power production, based on ~~MAE reduction during a 1-week comparison with three extreme weather events. We forecasted three storms in February 2022 while also representing the error reduction during four selected study cases. The simulation results included~~ wind farms in the

615 domain. ~~The swift nature of these extreme events was captured, and we further enhanced the predictions using FDDA of in-situ (SCADA) observations: improvements were observed regardless of the flow direction.~~

One of the study cases involved two extreme weather events in February 2022, which were captured well by the simulations. Moreover, we explored the leverage of the FDDA method in a ~~day-ahead day-long~~ frame by assimilating data either from an ~~upstream upwind~~ (WHi) LiDAR at a specific height, or solely from SCADA at hub height. We performed ~~11 a~~ sensitivity study

620 via 18 numerical experiments that have eight different values for radius of influence of DA, as well as ~~three five different~~ values for nudging strength. This helped to identify an optimal FDDA configuration for this offshore setting. We highlighted the benefits of having an ~~upstream upwind~~ LiDAR, as its assimilation improves ~~predictions downstream results 47 km downwind~~ at the location of the wind farm. To benefit from this configuration, the only requirement is to have the most common wind direction (which for the Southern Bight of the North Sea ~~, this is from South-West) incoming to the Westhinder LiDAR.~~ The

625 experiments of ~~upstream LiDAR DA upwind LiDAR FDDA~~ exhibited improvements in ~~predictions results~~ which were quantified by MAEs, RMSEs, and bias, with respect to the local observations. The ~~MAEs for power production when assimilating upstream LiDAR are reduced approximately twice as compared to the simulations without any DA, whereas this reduction when assimilating SCADA is approximately four times~~ identified optimal FDDA setting was also applied to three more study cases. Furthermore, after demonstrating the leverage of ~~upstream DA upwind nudging~~, we explored a forecasting routine that

630 contains ~~eyelical cyclic~~ nudging windows, which also showed ~~improved forecasts~~ improvements in hour-ahead predictions that were quantified via MAEs.

Limitations of this work include the requirement for a specific range of values for wind direction: the assimilation of Westhinder LiDAR data would not show improvements in the downstream region of interest if the wind direction is not from South-West. Additionally, the lack of offshore observations (especially in real-time) due to the harsh offshore conditions that

635 impact measurement campaigns (as well as cost of deployment, maintenance, structural limitations in deeper waters) reduces the geographical areas in which this method can be applied. Another important limitation is that only prognostic variables can be assimilated with the FDDA method, which is why variational methods are widely used and hold potential for future works. ~~Furthermore, the~~ It is worth mentioning that the nudging of waked turbines can affect the physical evolution of turbine and farm wakes at typical mesoscale resolutions that do not resolve individual turbine wakes. A detailed study on this is left for

640 future work. Furthermore, with the increasing density of wind farms installed in the North Sea, the assimilation of SCADA data from neighboring wind farms in NWP models is an important topic for future research.

The methods in this work can be valuable in the future for ~~operational nowcasting, as well as for~~ long-term refined reanalysis (several weeks to few years), where the assimilation of offshore data acquired during wind farm pre-development phase can help reduce bias errors and/or reduce the risk of under-sampling extremes, or where the goal is to evaluate the effects of wind farm decommission on present farms.

Practical implications for the wind energy industry can be derived from this research: by utilizing open-source NWP models such as WRF, which is designed for both atmospheric research and operational forecasting applications, more informed wind farm planning and decision-making strategies can be pursued, even under extreme weather conditions. This is especially feasible if offshore measurement campaigns continue to be motivated. ~~Furthermore, with the increasing density of wind farms installed in the North Sea, the assimilation of SCADA data from neighboring wind farms in NWP models is an important topic for future research.~~

Code and data availability. The Advanced Research WRF (ARW) model is developed by the National Center for Atmospheric Research, (Skamarock et al., 2019). WRF v4.5.1 is publicly available at <https://github.com/wrf-model/WRF/releases/tag/v4.5.1> (last accessed: September 2023). The forcing data used for initial and boundary conditions in the WRF simulations is also publicly available at the NCEP GFS 0.25 Degree Global Forecast Grids Historical Archive, DOI: 10.5065/D65D8PWK. Data from the numerical simulations and the namelists used in the WRF model are available upon reasonable requests. The postprocessing routines are built using the wrf-python library (Ladwig, 2017). The Westhinder LiDAR data is collected in the framework of the SeaFD project, funded by the Fund for Innovation and Entrepreneurship (VLAIO) at the von Karman Institute for Fluid Dynamics. The LiDAR datasets at the Lichteiland Goeree platform and at the Europlatform are available thanks to the Wind@Sea project, Wind Energy Research Group at TNO Energy Transition (<https://www.tno.nl/>, <https://nimbus.windopzee.net/>). Finally, the SCADA observations of the wind farm of interest, as well as details regarding the wind turbines, are under a non-disclosure agreement (NDA).

Appendix A: Included wind farms in the numerical setup

The included wind farms in the numerical setup are described ~~hereafter,~~ in Table A1, using data from Hoeser et al. (2022) and Hoeser and Kuenzer (2022).

665 Appendix B: Supplementary color maps of errors for wind direction and power in F2

To support the findings on optimal FDDA settings based on wind speed error reduction in Sect. 3.1, we include the errors for wind direction and power. Figure B1 contains wind direction RMSEs and biases that showcase significant improvements when FDDA is performed (especially for the preferred configurations L04 and L06). Figure B2 displays power improvements for RMSE and bias for all FDDA configurations that have an active WFP. These improvements are quite significant, considering the (almost twice as high) error values in the case 'F2, WFP' (when no data is assimilated). The results in both figures are consistent with the analysis in Sect. 3.1.

Table A1. [Details on wind farms \(Isited in no particular order\) in the Southern Bight of the North Sea summarized from Hoeser et al. \(2022\)](#)

Wind farm name	Total number of turbines (#)	Turbine Capacity	Hub Height (m)	Rotor Diameter (m)
Borssele I	94	8.4 MW	107	164
Borssele II				
Borssele III				
Borssele IV				
Borssele V				
Throntonbank I	48	6.15 MW	93.3	126
Throntonbank II & III				
Rentel	42	7.35 MW	102	154
Northwind	72	3.0 MW	80.1	112
SeaMade (Seastar)	30	8.4 MW	107	164
Norther	44	8.4 MW	107	164
Nobelwind	50	3.3 MW	77.1	112
Belwind	55	3.0 MW	70.1	112
Belwind Alstom Hailiade	1	6.0 MW	98.1	150
Northwester 2	23	9.5 MW	107	164
Seamade (Mermaid)	28	8.4 MW	107	164
Scroby Sands	30	2.0 MW	68	80
East Anglia ONE	102	7 MW	120	154
Galloper	56	6 MW	88	154
Greater Gabbard	140	3.6 MW	78	107
Gunfleet Sands	48	3.6 MW	78	107
Gunfleet Sands	2	6 MW	84	120
London Array	175	3.6 MW	87	120
Kentfish Flats	30	3 MW	70	90
Kentfish Flats	15	3.3 MW	83.6	112
Thanet	100	3 MW	70	90
Luchterduinen	43	3 MW	81	112
Egmond aan Zee	36	3 MW	70	90
Princess Amalia	60	2 MW	60	80

[Details](#)

[on wind farms \(Isited in no particular order\) in the Southern Bight of the North Sea summarized from Hoeser et al. \(2022\).](#)

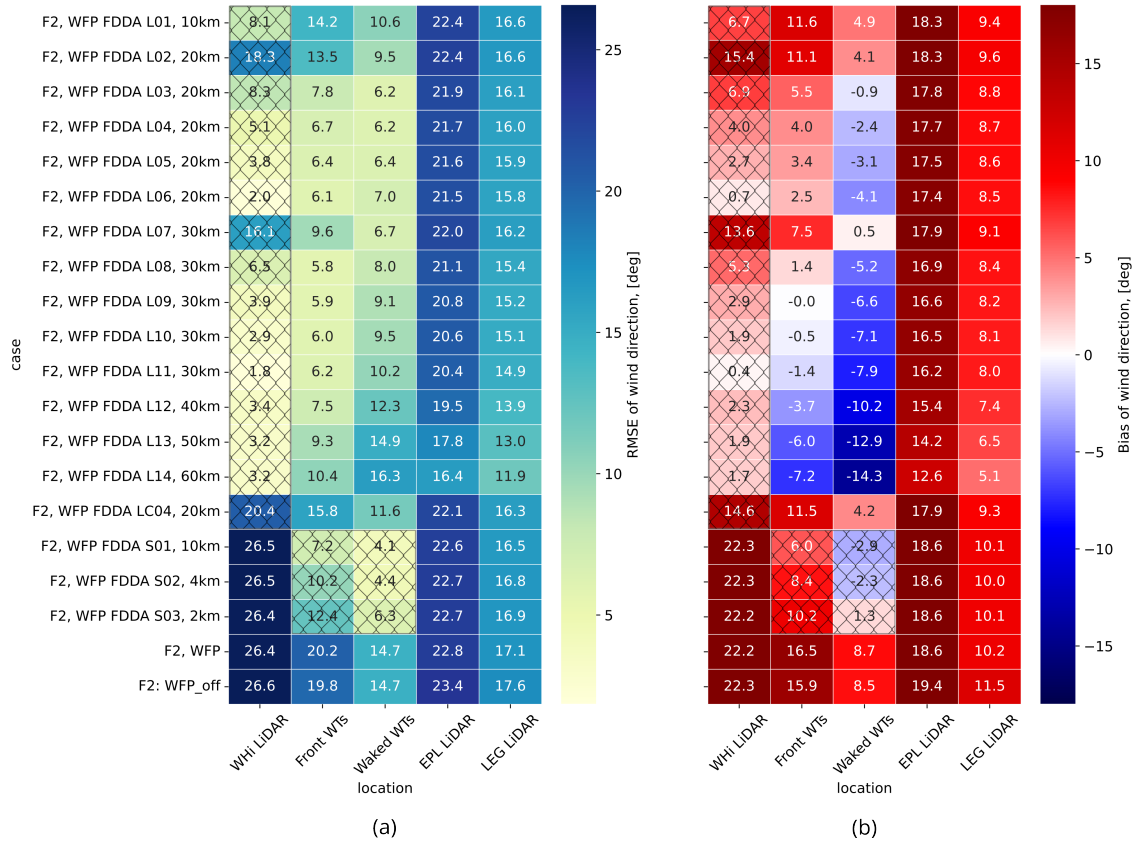


Figure B1. Color maps of MAE (a) and bias (b) for wind direction for the different simulations computed at the five locations with respect to the corresponding observations: WHi at 104.5 m, EPL at 116 m, LEG at 115 m, and Front and Waked WTs at hub height. Results at assimilation locations are marked with crossed-out cells.

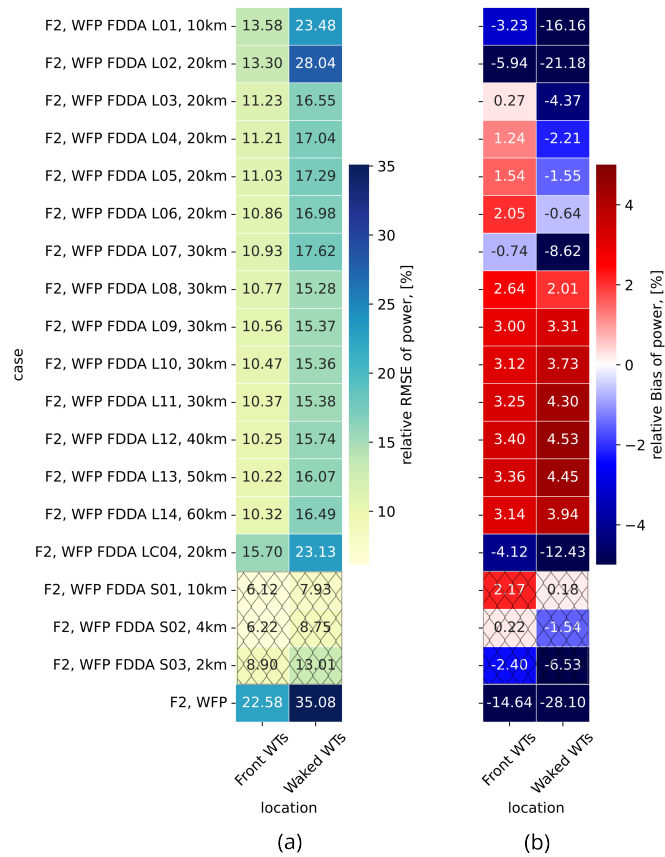


Figure B2. Color maps of MAE (a) and bias (b) for power for the different simulations (with an active WFP) computed at the two wind farm locations (Front and Waked WTs) at hub height. Results at assimilation locations are marked with crossed-out cells.

Author contributions. Tsvetelina Ivanova: Conceptualization (equal); Data curation (lead); Formal analysis (lead); Investigation (lead); Methodology (lead); Software (lead); Visualization (lead); Writing – original draft preparation (lead); Writing – review & editing (lead).

675 Sara Porchetta: Formal analysis (equal); Investigation (equal); Methodology (equal); Supervision (equal); Validation (equal); Writing – review & editing (equal).

Sophia Buckingham: Funding acquisition (equal); Methodology (equal); Resources (equal); Writing – review & editing (equal).

Gertjan Glabeke: Investigation (equal); Writing – review & editing (equal).

Jeroen van Beeck: Funding acquisition (equal); Methodology (equal); Resources (equal); Writing – review & editing (equal).

680 Wim Munters: Conceptualization (lead); Formal analysis (equal); Funding acquisition (lead); Investigation (equal); Methodology (equal); Project administration (lead); Resources (lead); Supervision (lead); Writing – review & editing (equal).

Competing interests. The authors declare that no competing interests are present.

Acknowledgements. The authors acknowledge the RAINBOW and SeaFD projects, funded by Flanders Innovation & Entrepreneurship (VLAIO) of the Flemish Government. Furthermore, the authors acknowledge ~~support by~~ the BeFORECAST project, which is supported by the Energy Transition Fund of the Belgian Federal Government.

685 ~~The authors extend their gratitude to Pieter Mathys from the von Karman Institute for the review and support during the preparation of the manuscript. The authors acknowledge and thank Gertjan Glabeke from the von Karman Institute for processing the Westhinder LiDAR data.~~

~~Furthermore, the authors express acknowledgements and gratitude to the~~ Acknowledgements go towards the Wind@Sea project, Wind Energy Research Group at TNO Energy Transition (<https://www.tno.nl/>, <https://nimbus.windopzee.net/>), for the available LiDAR observations at the Lichteiland Goeree platform and at the Europlatform. The authors extend their gratitude to Pieter Mathys from the von Karman Institute for the review and support during the preparation of the manuscript.

690

The results in this paper are obtained using free and open-source software: the authors extend their gratitude to the communities that have built these powerful tools from which everyone can benefit.

695 Finally, Tsvetelina Ivanova would like to thank Emmanuel Gillyns ~~from the von Karman Institute,~~ for the valuable feedback regarding ~~the structure of~~ the manuscript.

References

- Ali, K., Schultz, D. M., Revell, A., Stallard, T., and Ouro, P.: Assessment of Five Wind-Farm Parameterizations in the Weather Research and Forecasting Model: A Case Study of Wind Farms in the North Sea, *Monthly Weather Review*, 151, 2333–2359, <https://doi.org/10.1175/mwr-d-23-0006.1>, 2023.
- 700 Archer, C. L., Colle, B. A., Delle Monache, L., Dvorak, M. J., Lundquist, J., Bailey, B. H., Beaucage, P., Churchfield, M. J., Fitch, A. C., Kosovic, B., Lee, S., Moriarty, P. J., Simao, H., Stevens, R. J. A. M., Veron, D., and Zack, J.: Meteorology for Coastal/Offshore Wind Energy in the United States: Recommendations and Research Needs for the Next 10 Years, *Bulletin of the American Meteorological Society*, 95, 515–519, <https://doi.org/10.1175/bams-d-13-00108.1>, 2014.
- Archer, C. L., Wu, S., Ma, Y., and Jiménez, P. A.: Two Corrections for Turbulent Kinetic Energy Generated by Wind Farms in the WRF
705 Model, *Monthly Weather Review*, 148, 4823–4835, <https://doi.org/10.1175/mwr-d-20-0097.1>, 2020.
- Barker, D., Huang, X.-Y., Liu, Z., Auligné, T., Zhang, X., Rugg, S., Ajjaji, R., Bourgeois, A., Bray, J., Chen, Y., Demirtas, M., Guo, Y.-R., Henderson, T., Huang, W., Lin, H.-C., Michalakes, J., Rizvi, S., and Zhang, X.: The Weather Research and Forecasting Model's Community Variational/Ensemble Data Assimilation System: WRFDA, *Bulletin of the American Meteorological Society*, 93, 831–843, <https://doi.org/10.1175/bams-d-11-00167.1>, 2012.
- 710 Barker, D. M., Huang, W., Guo, Y.-R., Bourgeois, A. J., and Xiao, Q. N.: A Three-Dimensional Variational Data Assimilation System for MM5: Implementation and Initial Results, *Monthly Weather Review*, 132, 897–914, [https://doi.org/10.1175/1520-0493\(2004\)132<0897:atvdas>2.0.co;2](https://doi.org/10.1175/1520-0493(2004)132<0897:atvdas>2.0.co;2), 2004.
- Belgian Offshore Platform News: Stormy February drives offshore energy production to new record, Available at: <https://www.belgianoffshoreplatform.be/en/news/stormy-february-drives-offshore-energy-production-to-new-record/> (Accessed: August 23rd, 2023),
715 2022.
- Cheng, W. Y., Liu, Y., Liu, Y., Zhang, Y., Mahoney, W. P., and Warner, T. T.: The impact of model physics on numerical wind forecasts, *Renewable Energy*, 55, 347–356, <https://doi.org/10.1016/j.renene.2012.12.041>, 2013.
- Cheng, W. Y., Liu, Y., Bourgeois, A. J., Wu, Y., and Haupt, S. E.: Short-term wind forecast of a data assimilation/weather forecasting system with wind turbine anemometer measurement assimilation, *Renewable Energy*, 107, 340–351,
720 <https://doi.org/10.1016/j.renene.2017.02.014>, 2017.
- Dörenkämper, M., Olsen, B. T., Witha, B., Hahmann, A. N., Davis, N. N., Barcons, J., Ezber, Y., García-Bustamante, E., González-Rouco, J. F., Navarro, J., Sastre-Marugán, M., Sile, T., Trei, W., Žagar, M., Badger, J., Gottschall, J., Rodrigo, J. S., and Mann, J.: The Making of the New European Wind Atlas - Part 2: Production and evaluation, *Geoscientific Model Development*, 13, 5079–5102, <https://doi.org/10.5194/gmd-13-5079-2020>, 2020.
- 725 Ek, M. B., Mitchell, K. E., Lin, Y., Rogers, E., Grunmann, P., Koren, V., Gayno, G., and Tarpley, J. D.: Implementation of Noah land surface model advances in the National Centers for Environmental Prediction operational mesoscale Eta model, *Journal of Geophysical Research: Atmospheres*, 108, <https://doi.org/10.1029/2002jd003296>, 2003.
- Eriksson, O., Baltscheffsky, M., Breton, S.-P., Söderberg, S., and Ivanell, S.: The Long distance wake behind Horns Rev I studied using large eddy simulations and a wind turbine parameterization in WRF, *Journal of Physics: Conference Series*, 854, 012012,
730 <https://doi.org/10.1088/1742-6596/854/1/012012>, 2017.
- Fischereit, J., Brown, R., Larsén, X. G., Badger, J., and Hawkes, G.: Review of Mesoscale Wind-Farm Parametrizations and Their Applications, *Boundary-Layer Meteorology*, 182, 175–224, <https://doi.org/10.1007/s10546-021-00652-y>, 2022a.

- Fischereit, J., Hansen, K. S., Larsén, X. G., van der Laan, M. P., Réthoré, P.-E., and Leon, J. P. M.: Comparing and validating intra-farm and farm-to-farm wakes across different mesoscale and high-resolution wake models, *Wind Energy Science*, 7, 1069–1091, <https://doi.org/10.5194/wes-7-1069-2022>, 2022b.
- 735 Fitch, A. C., Olson, J. B., Lundquist, J. K., Dudhia, J., Gupta, A. K., Michalakes, J., and Barstad, I.: Local and mesoscale impacts of wind farms as parameterized in a mesoscale NWP model, *Monthly Weather Review*, 140, 3017–3038, <https://doi.org/10.1175/MWR-D-11-00352.1>, 2012.
- Glabeke, G., Buckingham, S., De Mulder, T., and van Beeck, J.: Anomalous wind events over the Belgian North Sea at heights relevant to wind energy, <https://zenodo.org/record/8034397>, Wind Energy Science Conference 2023 Mini-Symposium 1.5 IEA Wind Task 52: Replacing met masts and Accelerating offshore wind deployment, Submission Number 438, 2023.
- 740 Grell, G. A., Dudhia, J., Stauffer, D. R., et al.: A description of the fifth-generation Penn State/NCAR Mesoscale Model (MM5), 1994.
- Hahmann, A. N., Sile, T., Witha, B., Davis, N. N., Dörenkämper, M., Ezber, Y., García-Bustamante, E., González-Rouco, J. F., Navarro, J., Olsen, B. T., and Söderberg, S.: The making of the New European Wind Atlas - Part 1: Model sensitivity, *Geoscientific Model Development*, 13, 5053–5078, <https://doi.org/10.5194/gmd-13-5053-2020>, 2020.
- 745 Hoerer, T. and Kuenzer, C.: DeepOWT: A global offshore wind turbine data set, <https://doi.org/10.5281/ZENODO.5933967>, 2022.
- Hoerer, T., Feuerstein, S., and Kuenzer, C.: DeepOWT: A global offshore wind turbine data set derived with deep learning from Sentinel-1 data, <https://doi.org/10.5194/essd-2022-115>, preprint, 2022.
- Huang, X.-Y., Xiao, Q., Barker, D. M., Zhang, X., Michalakes, J., Huang, W., Henderson, T., Bray, J., Chen, Y., Ma, Z., Dudhia, J., Guo, Y., Zhang, X., Won, D.-J., Lin, H.-C., and Kuo, Y.-H.: Four-Dimensional Variational Data Assimilation for WRF: Formulation and Preliminary Results, *Monthly Weather Review*, 137, 299–314, <https://doi.org/10.1175/2008mwr2577.1>, 2009.
- 750 Iacono, M. J., Delamere, J. S., Mlawer, E. J., Shephard, M. W., Clough, S. A., and Collins, W. D.: Radiative forcing by long-lived greenhouse gases: Calculations with the AER radiative transfer models, *Journal of Geophysical Research*, 113, <https://doi.org/10.1029/2008jd009944>, 2008.
- 755 Kain, J. S.: The Kain–Fritsch Convective Parameterization: An Update, *Journal of Applied Meteorology*, 43, 170–181, [https://doi.org/10.1175/1520-0450\(2004\)043<0170:tkcpau>2.0.co;2](https://doi.org/10.1175/1520-0450(2004)043<0170:tkcpau>2.0.co;2), 2004.
- Kosovic, B., Haupt, S. E., Adriaansen, D., Alessandrini, S., Wiener, G., Monache, L. D., Liu, Y., Linden, S., Jensen, T., Cheng, W., Politovich, M., and Prestopnik, P.: A Comprehensive Wind Power Forecasting System Integrating Artificial Intelligence and Numerical Weather Prediction, *Energies*, 13, 1372, <https://doi.org/10.3390/en13061372>, 2020.
- 760 Ladwig, B.: wrf-python (Version 1.3.4) [Software], <https://doi.org/10.5065/D6W094P1>, Boulder, Colorado: UCAR/NCAR, 2017.
- Larsén, X. G. and Fischereit, J.: A case study of wind farm effects using two wake parameterizations in the Weather Research and Forecasting (WRF) model (V3.7.1) in the presence of low-level jets, *Geoscientific Model Development*, 14, 3141–3158, <https://doi.org/10.5194/gmd-14-3141-2021>, 2021.
- Larsén, X. G., Du, J., Bolaños, R., Imberger, M., Kelly, M. C., Badger, M., and Larsen, S.: Estimation of offshore extreme wind from wind-wave coupled modeling, *Wind Energy*, <https://doi.org/10.1002/we.2339>, 2019.
- 765 Lee, J. C. Y. and Lundquist, J. K.: Evaluation of the wind farm parameterization in the Weather Research and Forecasting model (version 3.8.1) with meteorological and turbine power data, *Geoscientific Model Development*, 10, 4229–4244, <https://doi.org/10.5194/gmd-10-4229-2017>, 2017.
- Liu, Y., Warner, T. T., Bowers, J. F., Carson, L. P., Chen, F., Clough, C. A., Davis, C. A., Egeland, C. H., Halvorson, S. F., Huck, T. W., Lachapelle, L., Malone, R. E., Rife, D. L., Sheu, R.-S., Swerdlin, S. P., and Weingarten, D. S.: The Operational Mesogamma-
- 770

- Scale Analysis and Forecast System of the U.S. Army Test and Evaluation Command. Part I: Overview of the Modeling System, the Forecast Products, and How the Products Are Used, *Journal of Applied Meteorology and Climatology*, 47, 1077–1092, <https://doi.org/10.1175/2007jamc1653.1>, 2008.
- 775 Lydia, M., Kumar, S. S., Selvakumar, A. I., and Kumar, G. E. P.: A comprehensive review on wind turbine power curve modeling techniques, *Renewable and Sustainable Energy Reviews*, 30, 452–460, <https://doi.org/10.1016/j.rser.2013.10.030>, 2014.
- Mylonas, M., Barbouchi, S., Herrmann, H., and Nastos, P.: Sensitivity analysis of observational nudging methodology to reduce error in wind resource assessment (WRA) in the North Sea, *Renewable Energy*, 120, 446–456, <https://doi.org/10.1016/j.renene.2017.12.088>, 2018.
- Nakanishi, M. and Niino, H.: An Improved Mellor–Yamada Level-3 Model: Its Numerical Stability and Application to a Regional Prediction of Advection Fog, *Boundary-Layer Meteorology*, 119, 397–407, <https://doi.org/10.1007/s10546-005-9030-8>, 2006.
- 780 National Centers for Environmental Prediction, National Weather Service, NOAA, U.S. Department of Commerce: NCEP GFS 0.25 Degree Global Forecast Grids Historical Archive, <https://doi.org/10.5065/D65D8PWK>, 2015.
- Peña, A., Mirocha, J. D., and van der Laan, M. P.: Evaluation of the Fitch Wind-Farm Wake Parameterization with Large-Eddy Simulations of Wakes Using the Weather Research and Forecasting Model, *Monthly Weather Review*, 150, 3051–3064, <https://doi.org/10.1175/mwr-d-22-0118.1>, 2022.
- 785 Porchetta, S., Muñoz-Esparza, D., Munters, W., van Beeck, J., and van Lipzig, N.: Impact of ocean waves on offshore wind farm power production, *Renewable Energy*, 180, 1179–1193, <https://doi.org/10.1016/j.renene.2021.08.111>, 2021.
- Pryor, S. C. and Barthelmie, R. J.: A global assessment of extreme wind speeds for wind energy applications, *Nature Energy*, 6, 268–276, <https://doi.org/10.1038/s41560-020-00773-7>, 2021.
- Reen, B.: A Brief Guide to Observation Nudging in WRF, 2016.
- 790 Sethunadh, J., Letson, F. W., Barthelmie, R. J., and Pryor, S. C.: Assessing the impact of global warming on windstorms in the northeastern United States using the pseudo-global-warming method, *Natural Hazards*, 117, 2807–2834, <https://doi.org/10.1007/s11069-023-05968-1>, 2023.
- Skamarock, W. C. and Klemp, J. B.: A time-split nonhydrostatic atmospheric model for weather research and forecasting applications, *Journal of Computational Physics*, 227, 3465–3485, <https://doi.org/10.1016/j.jcp.2007.01.037>, 2008.
- 795 Skamarock, W. C., Klemp, J. B., Dudhia, J., Gill, D. O., Liu, Z., Berner, J., Wang, W., Powers, J. G., Duda, M. G., Barker, D. M., and Huang, X.-Y.: A Description of the Advanced Research WRF Model Version 4.3, <https://doi.org/10.5065/1DFH-6P97>, 2019.
- Soman, S. S., Zareipour, H., Malik, O., and Mandal, P.: A review of wind power and wind speed forecasting methods with different time horizons, in: *North American Power Symposium 2010*, IEEE, <https://doi.org/10.1109/naps.2010.5619586>, 2010.
- Sun, W., Liu, Z., Song, G., Zhao, Y., Guo, S., Shen, F., , and Sun, X.: Improving Wind Speed Forecasts at Wind Turbine Locations over Northern China through Assimilating Nacelle Winds with WRFDA, *Weather and Forecasting*, 37, 545–562, <https://doi.org/10.1175/WAF-D-21-0041.1>, 2022.
- 800 Thompson, G., Field, P. R., Rasmussen, R. M., and Hall, W. D.: Explicit Forecasts of Winter Precipitation Using an Improved Bulk Microphysics Scheme. Part II: Implementation of a New Snow Parameterization, *Monthly Weather Review*, 136, 5095–5115, <https://doi.org/10.1175/2008mwr2387.1>, 2008.
- Tomaszewski, J. M. and Lundquist, J. K.: Observations and simulations of a wind farm modifying a thunderstorm outflow boundary, *Wind Energy Science*, 6, 1–13, <https://doi.org/10.5194/wes-6-1-2021>, 2021.

- Vemuri, A., Buckingham, S., Munters, W., Helsen, J., and van Beeck, J.: Sensitivity analysis of mesoscale simulations to physics parameterizations over the Belgian North Sea using Weather Research and Forecasting – Advanced Research WRF (WRF-ARW), *Wind Energy Science*, 7, 1869–1888, <https://doi.org/10.5194/wes-7-1869-2022>, 2022.
- 810 Wang, Y., Hu, Q., Li, L., Foley, A. M., and Srinivasan, D.: Approaches to wind power curve modeling: A review and discussion, *Renewable and Sustainable Energy Reviews*, 116, 109–122, <https://doi.org/10.1016/j.rser.2019.109422>, 2019.
- Wind@Sea project, Wind Energy Research Group at TNO Energy Transition: LiDAR measurements at Lichteiland Goeree (LEG) and at Europlatform (EPL), (<https://www.tno.nl/>, <https://nimbus.windopzee.net/>), 2023.
- Xu, M., Liu, Y., Davis, C. A., and Warner, T. T.: Sensitivity study on nudging parameters for a mesoscale FDDA system, in: CONFERENCE ON WEATHER ANALYSIS AND FORECASTING, vol. 19, pp. 127–130, AMS, 2002.
- 815 Yang, B., Zhong, L., Wang, J., Shu, H., Zhang, X., Yu, T., and Sun, L.: State-of-the-art one-stop handbook on wind forecasting technologies: An overview of classifications, methodologies, and analysis, *Journal of Cleaner Production*, 283, 124–162, <https://doi.org/10.1016/j.jclepro.2020.124628>, 2021.
- ZephIR: ZephIR Lidar 2018 WALTZ - a user's guide, version 2.2, 2018.
- 820 Zhang, X., Huang, X.-Y., and Pan, N.: Development of the Upgraded Tangent Linear and Adjoint of the Weather Research and Forecasting (WRF) Model, *Journal of Atmospheric and Oceanic Technology*, 30, 1180–1188, <https://doi.org/10.1175/jtech-d-12-00213.1>, 2013.
- Zhang, X., Huang, X.-Y., Liu, J., Poterjoy, J., Weng, Y., Zhang, F., and Wang, H.: Development of an Efficient Regional Four-Dimensional Variational Data Assimilation System for WRF, *Journal of Atmospheric and Oceanic Technology*, 31, 2777–2794, <https://doi.org/10.1175/jtech-d-13-00076.1>, 2014.
- 825 Zhao, X., Wang, S., and Li, T.: Review of Evaluation Criteria and Main Methods of Wind Power Forecasting, *Energy Procedia*, 12, 761–769, <https://doi.org/10.1016/j.egypro.2011.10.102>, 2011.